www.acsnano.org

Harnessing Surface Hydrophilicity of Inhalable Nanoparticles for Precision Delivery of Glucagon-like Peptide-1 Receptor Agonists or Anti-Asthmatic Therapeutics

Xi Liu, Lie Zhang, Sa Li, Liyun Xing, Mingjie Ni, Minyi Huang, and Yuan Huang*



Downloaded via SICHUAN UNIV on June 29, 2025 at 02:25:59 (UTC). See https://pubs.acs.org/sharingguidelines for options on how to legitimately share published articles.

Cite This: ACS Nano 2025, 19, 22357-22375



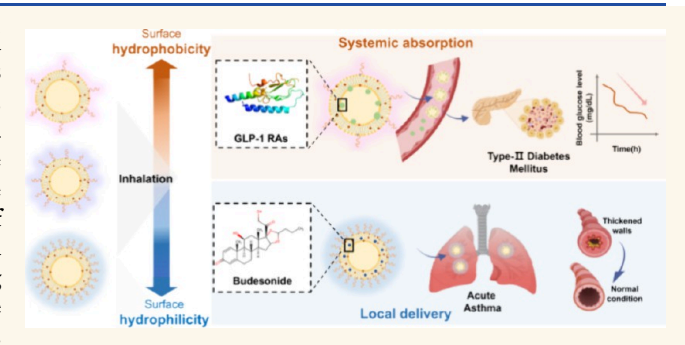
ACCESS I

III Metrics & More

Article Recommendations

s Supporting Information

ABSTRACT: Rational adjustment of surface physicochemical properties of inhalable nanocarriers significantly influences their in vivo fate during pulmonary delivery. Among these, surface hydrophilicity/hydrophobicity has been recognized as a critical factor in the transmucosal process. However, the impacts of surface hydrophilicity/hydrophobicity on the transcellular performance and ultimate therapeutic effects of pulmonary-delivered nanosystems still remain unelucidated. In this study, we developed a series of liposomes with varying surface hydrophilicity to investigate the effect of surface properties on both local and systemic drug delivery.



Interestingly, low-hydrophilic liposomes exhibited enhanced systemic absorption, whereas high-hydrophilic liposomes demonstrated prolonged pulmonary residence after inhalation. To validate this principle, we applied two disease models. In a type II diabetes mellitus model, low hydrophilic liposomes loaded with GLP-1 receptor agonists (Liraglutide or Semaglutide) showed excellent systemic drug delivery and hypoglycemic effects. In an OVA-induced allergic asthma model, budesonide-loaded high hydrophilic liposomes significantly alleviated symptoms while reducing dosing frequency. Mechanistic studies further revealed that liposomes with lower surface hydrophilicity could enhance the transcellular transport efficiency of the drug through alveolar epithelial cells, while those with higher surface hydrophilicity prolonged the pulmonary residence of the drug by decreasing alveolar epithelium transportation and the avoidance of macrophage clearance. Lastly, we evaluated the biocompatibility of these liposomes following inhalation. Overall, tuning the surface hydrophilicity/hydrophobicity of inhalable nanocarriers to suit local or systemic delivery goals offers valuable insights for the rational design of advanced pulmonary delivery systems.

KEYWORDS: pulmonary delivery, inhalable liposome, surface hydrophilicity/hydrophobicity, systemic absorption, respiratory disease, GLP-1RAs, budesonide

1. INTRODUCTION

In recent years, the pulmonary route of drug delivery has gained huge interest in scientific and industrial fields and is explored widely for local and systemic drug delivery for the treatment of various diseases, including pulmonary and nonpulmonary diseases. The high permeability and surface area, rich blood supply of the lung provide an alternative route for drug delivery in ailments such as asthma, chronic obstructive pulmonary disease, and diabetes. Early in the 21st century, some researchers attempted to develop inhalable formulations for systemic delivery of macromolecular drugs, such as insulin and calcitonin, which showed relative bioavailability rates of up to 20%. Beyond the systemic

delivery, inhalable formulations offer great opportunities for treating various pulmonary diseases due to the significantly augmented drug accumulation and stability in a mild physiological environment. Additionally, the COVID-19 pandemic further propelled the demand for inhalable therapies. ^{10–12} Although the pulmonary mucosa possesses

Received: April 5, 2025 Revised: May 27, 2025 Accepted: May 28, 2025 Published: June 9, 2025





numerous conveniences for drug delivery, successful delivery of inhaled formulation still encounters considerable challenges from the powerful clearance mechanism and physiologic barriers of lung tissue. ^{8,13,14}

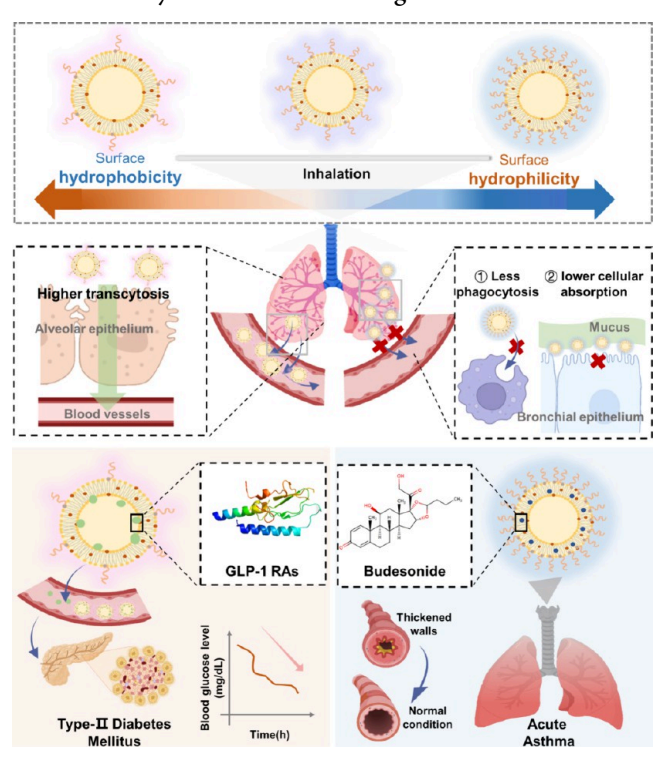
In general, effective lung deposition is a critical first step for both local and systemic drug delivery via inhalation. This ensures that the drug reaches the lungs rather than being trapped in the upper airways or exhaled. Once deposited, drugs confront major barriers, including clearance by mucociliary mechanisms and alveolar macrophages. Additionally, inhaled drugs need to traverse the alveolar epithelium and undergo complex intracellular trafficking before entering into blood circulation. Meanwhile, the presence of metabolic enzymes might result in the degradation of biomacromolecule drugs, as well. All of these conditions severely hindered the delivery efficiency and therapeutic effects of inhaled drugs.

During the recent 20-30 years, the emergence of nanotechnology has revolutionized the field of pulmonary delivery systems. $^{15-17}$ On the one hand, nanoscale delivery systems enable effective deep lung deposition and improve the in vivo stability of drugs. On the other hand, the tunable physicochemical properties of nanocarriers make them versatile tools for a wide range of applications. Recent studies highlight the crucial roles of the physicochemical properties of nanocarriers in their interplays with the delivery environment, comprising particle size, surface charge, rigidity, and hydrophilicity/hydrophobicity. 18-23 It was reported that an increase in hydrophobicity of nanoparticles (NPs) would result in higher affinity to the cell membrane but shorter blood circulation. Our previous research also demonstrated that there must be a balance between the hydrophilicity and hydrophobicity on the surface of NPs, which would provide them with a rapid mucus-penetrating ability and satisfactory cellular uptake efficiency in the gastrointestinal tract.²⁴⁻ However, relevant investigations on pulmonary delivery systems are extremely limited. Only a few reports revealed that modulating surface hydrophilicity may improve the lung retention of nanocarriers by diminishing mucociliary clearance and alveolar macrophage phagocytosis. 28,29 The impacts of surface hydrophilicity/hydrophobicity on the transcellular performances and ultimate therapeutic effects of pulmonary delivered nanosystems still remain unelucidated. Therefore, it is urgent to comprehensively explore the role of surface hydrophilicity/hydrophobicity of nanocarriers on pulmonary delivery for local or systemic drug delivery.

Liposome is well-recognized as ideal nanocarrier with enhanced compatibility with pulmonary biology and flexible drug loading capability.^{30–32} Herein, we designed a series of liposomes with various surface hydrophilicity. An extensively used amphiphilic diblock copolymer, 1,2-distearoyl-sn-glycero-3-phosphoethanolamine-N-[methoxy(polyethylene glycol)-2000] (DSPE-PEG₂₀₀₀), was utilized to modulate surface hydrophilicity. Surprisingly, after inhalation, we found that liposomes with low surface hydrophilicity (LH Lip) exhibited superior systemic absorption, while those with high hydrophilicity (HH Lip) showed prolonged lung retention behaviors. Then two types of therapeutic agents were encapsulated separately. GLP-1 receptor agonists (Liraglutide and Semaglutide) for the treatment of type 2 diabetes, represented systemic delivery. 33,34 Budesonide (Bud) for the treatment of allergic asthma represents local lung delivery.³⁵ It is interesting that, after inhalation, GLP-1 receptor agonists (GLP-1 RAs) loaded LH Lip (GLP-1 RAs@LH Lip) elicited

excellent effects on diabetes, while budesonide loaded HH Lip (Bud@HH Lip) showed significant improvement on lung function with asthma, which is in agreement with their biodistribution results. Then comprehensive mechanism investigations were performed and the results showed that 1) lower surface hydrophilicity endowed liposomes with superior transcellular efficiency by regulating the entire process of endocytosis-intracellular trafficking-exocytosis in alveolar epithelial cells, 2) high surface hydrophilicity achieved long-term pulmonary residence through decreased alveolar epithelium transportation and admirable bypassing of macrophage clearance (shown in Scheme 1). Finally, the biocompatibility

Scheme 1. Schematic Illustration of Inhalable Liposomes with Different Surface Hydrophilicities for Systemic Delivery of GLP-1 Receptor Agonists (GLP-1 RAs) and Local Delivery of Anti-Asthma Drug^a



"Liposomes with different degrees of surface hydrophilicity were constructed via the addition of various amounts of DSPE-PEG₂₀₀₀. Then, after inhalation, lower hydrophilic liposomes (slightly hydrophobic liposomes) showed enhanced systemic absorption via superior trans-alveolar ability, while higher hydrophilic liposomes exhibited prolonged pulmonary retention by the effective bypassing of macrophage pinocytosis. Because of these features, liposomes with lower hydrophilicity generated excellent delivery efficiency of GLP-1 RAs (Liraglutide or Semaglutide) and significant hypoglycemic effects in type II diabetes mellitus mice with lad GLP-1 RAs. Higher hydrophilic liposomes effectively alleviate the therapeutic effects of budesonide in OVA-induced asthma mice. Scheme 1 was created using https://www.biorender.com with a license agreement.

of liposomes after inhaled delivery was investigated. In summary, by rationally adjusting the surface hydrophilicity and hydrophobicity of nanocarriers, local or systemic delivery could be achieved after inhalation. Our study offered valuable insights for the efficient and straightforward design of pulmonary delivery systems.

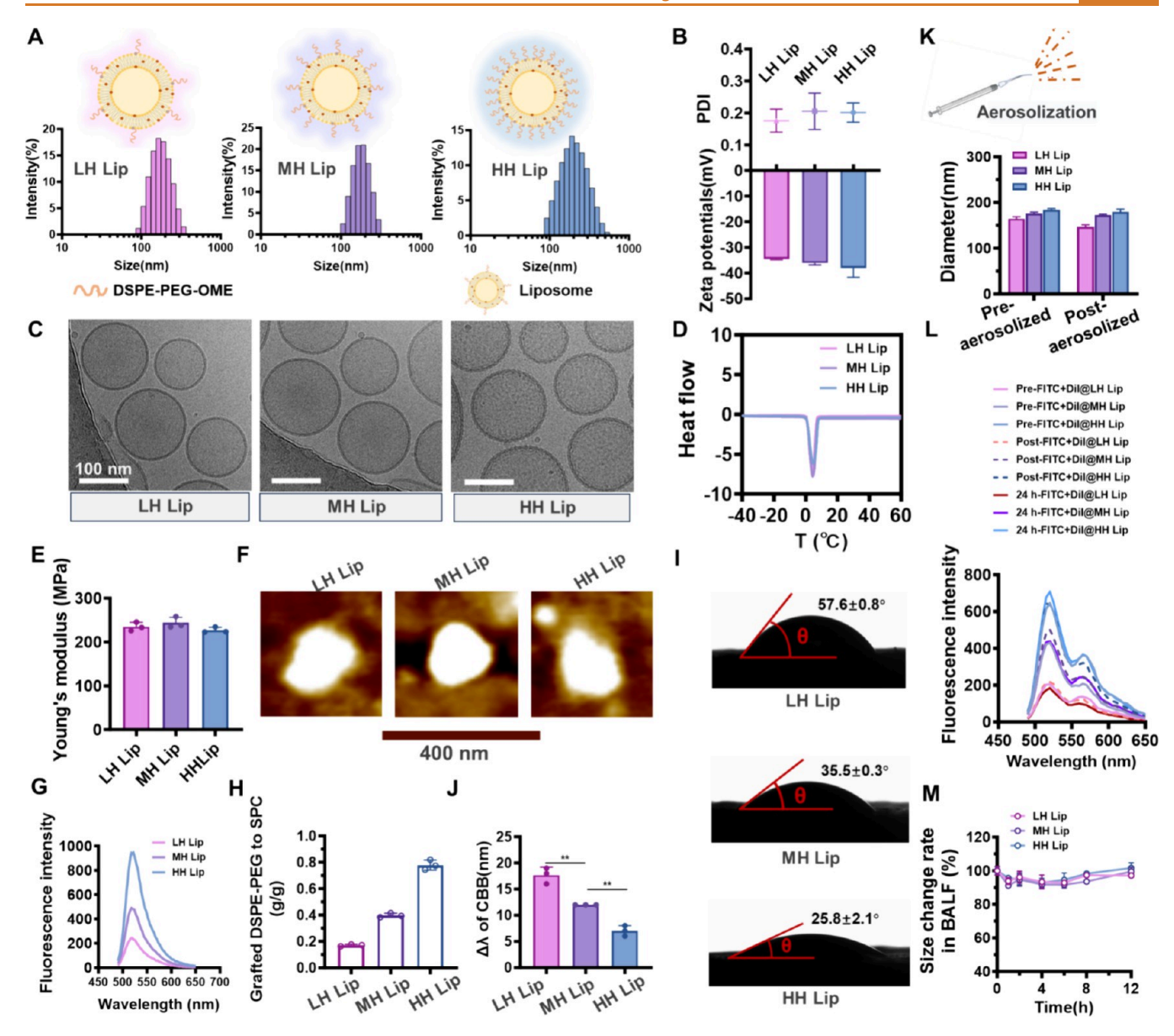


Figure 1. Preparation and characterization of liposomes with variable hydrophilicity. (A) Illustration and size distribution of liposomes with different surface hydrophilicity: LH Lip, MH Lip, and HH Lip. (B) Polydispersity index (PDI) and zeta potentials of liposomes with different surface hydrophilicity. (C) Cryo-TEM images of LH Lip, MH Lip, and HH Lip. Scale bar = 100 nm. (D) Differential scanning calorimetry (DSC) scan of liposomes with different hydrophilicity under the heating temperature of -40 to $60\,^{\circ}$ C. (E) Young's moduli of the liposomes with different hydrophilicity characterized by AFM, n = 3. (F) Corresponding deformation images of the liposomes with different hydrophilicity subjected to forces of different magnitudes by AFM, scale bar = $400\,\text{nm}$. (G) Fluorescence spectra of liposomes with different surface hydrophilicity prepared by FITC-labeled DSPE-PEG₂₀₀₀ at an excitation wavelength of 460 nm and emission wavelength of $490-620\,\text{nm}$. (H) Grafted ratios of DSPE-PEG₂₀₀₀ to lipid on the surfaces of liposomes with different hydrophilicity, n = 3. (I) Contact angle assays of liposomes with different hydrophilicity, n = 3. (J) Red shift values ($\Delta\lambda$) of Coomassie brilliant blue after incubation with LH Lip, MH Lip and HH Lip under the lipid concentration of 1.25 mg·mL⁻¹. Mean \pm SD (n = 3), (**) P < 0.01. (K) Diameters of liposomes with different hydrophilicity before and after atomization via a microsprayer aerosolizer, n = 3. (L) Fluorescence spectra of FITC+DiI dual-labeled liposomes (Pre-FITC+DiI@LH Lip, Pre-FITC+DiI@MH Lip, and Pre-FITC+DiI@HH Lip) after atomization (named Post-FITC+DiI@Lips) and 24 h incubation (named 24 h-FITC+DiI@Lips) with mouse-extracted BALF at an excitation wavelength of 460 nm and emission wavelength of 490–620 nm. (M) Particle size changes of liposomes in BALF over 12 h, n = 3. Labels (A, K) were created using https://www.biorender.com with a license agreement.

2. RESULTS AND DISCUSSION

2.1. Preparation and Characterization of Liposomes with Tunable Hydrophobicity. Liposome is widely utilized as a nanocarrier in drug delivery due to their biocompatibility, ease of preparation, and versatility in drug encapsulation. In this study, we aimed to develop liposomes with different surface hydrophilicity. To mitigate the potential degradation of

sensitive peptide drugs (GLP-1 RAs), we modified the commonly used two-step preparation method by replacing ultrasonication with extrusion to obtain liposomes. Additionally, we employed 1,2-distearoyl-sn-glycero-3-phosphoethanolamine-N-[methoxy(polyethylene glycol)-2000] (DSPE-PEG₂₀₀₀), a polymer known for its mucus-inert feature and

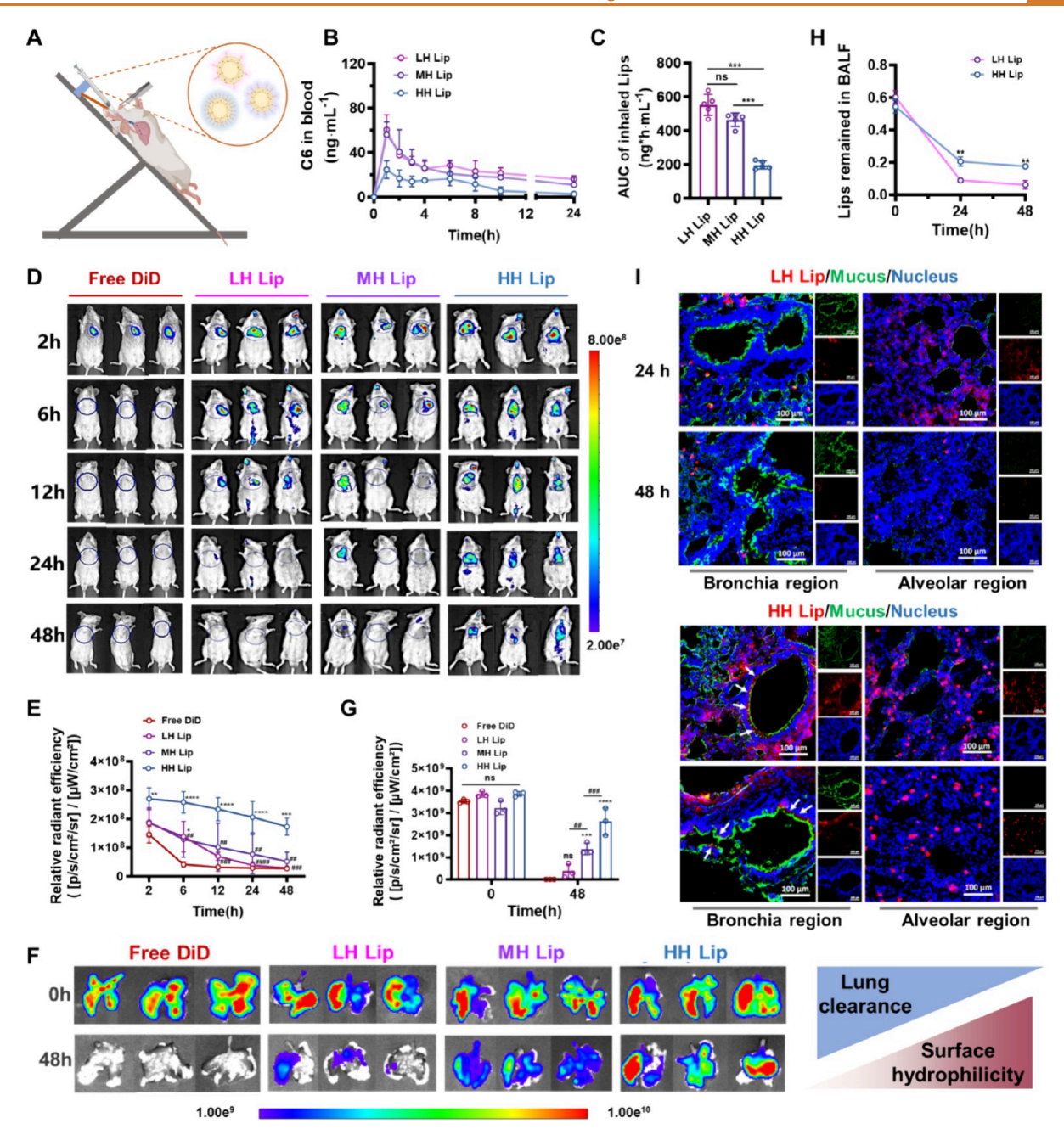


Figure 2. Surface hydrophobicity regulation defines the in vivo distribution of the inhaled liposomes. (A) Illustration of mice inhaled with liposome suspension via a microsprayer aerosolizer. During the experiment, mice were anesthetized and secured on a 45° inclined platform with their heads positioned upward and bodies kept upright. With the guidance of blunt forceps and laryngoscope, the microsprayer aerosolizer, preloaded with the liposome solution, was then inserted approximately 2.6 cm into the airway through the exposed tracheal opening, followed by a rapid injection (delivery volume $<50~\mu$ L) to complete the nebulization process. (B, C) Blood concentration profiles within 24 h and converted area under the curve (AUC) of LH Lip, MH Lip, and HH Lip loaded with the fluorescent dye Coumarin-6 (C6) after inhalation in mice, n = 5. (D, E) Real-time IVIS imaging and quantitative region-of-interest (ROI) analysis showing the distribution of inhaled DiD-labeled LH Lip, MH Lip, and HH Lip in normal mice, n = 3. (*, #) Mean group versus Free DiD and DiD@HH Lip at determined time point, respectively. (F, G) IVIS imaging and fluorescence quantification of lung tissues after 48 h inhalation with DiD-labeled LH Lip, MH Lip, and HH Lip, n = 3. (H) The DiI fluorescence intensity in bronchoalveolar lavage fluid (BALF) extracted from mice with 0, 24, and 48 h inhalation of liposomes with different hydrophilicity, n = 3. (*) Mean group versus DiD@LH Lip at determined time point, respectively. (I) Confocal images showing colocalization of mucus and liposomes with different hydrophilicity on lung tissues for 24 or 48 h incubation, Legend: red, DiI-labeled liposomes; green, AF488-labeled WGA, mucus; blue, nucleus. Statistical significance was calculated via one-way ANOVA, followed by Tukey's multiple comparison. (*, #) P < 0.005, (**, ##) P < 0.001, (***, ####) P < 0.0001.]. Label (A) was created using https://www.biorender.com with a license agreement.

ability to prolong NPs' circulation time, to modulate the surface hydrophilicity. $^{36-38}$

Three kinds of liposomes with different surface hydrophilicity (low hydrophilic liposome, intermediate hydrophilic liposome, and high hydrophilic liposome) were prepared using

different lipid-to-DSPE-PEG₂₀₀₀ ratios (10:2, 10:4, and 10:8), abbreviated as LH Lip, MH Lip, and HH Lip, respectively. Dynamic light scattering (DLS) analysis indicated that all liposomes had a consistent hydrated diameter of approximately 200 nm (Figure 1A) and a zeta potential of approximately –35 mV (Figure 1B). Cryo-transmission electron microscopy (TEM) images (Figure 1C) confirmed that all liposomes exhibited a uniformly typical closed vesicular structure with a bilayer membrane with an average size of 150 nm, regardless of the surface hydrophilicity.

Considering the potential influences of the various amounts of DSPE-PEG₂₀₀₀ on phage transition behaviors, differential scanning calorimetry (DSC) was employed to record the phase transition temperatures (T_m) of three liposomes under the heating temperature ranging from -40 to 60 °C. As shown in Figure 1D, T_m values for LH Lip, MH Lip, and HH Lip were 3.34, 3.38, and 3.56 °C, respectively. Compared to the liposomes with significantly different phase transition temperatures reported by Gan et al., the differences in $T_{\rm m}$ values among our three liposome formulations were negligible.³⁹ Additionally, atomic force microscopy (AFM) was used to measure Young's modulus of three liposome formulations (Figure 1E) and analyze their deformation morphology under identical applied pressure (Figure 1F). The results showed that all liposomes exhibited similar Young's modulus values (~225 MPa) with no significant differences. Moreover, their deformation under the same applied pressure was comparable, indicating that the increased DSPE-PEG₂₀₀₀ would not alter the rigidity of the liposomes.

Fluorescein isothiocyanate (FITC)-labeled DSPE-PEG₂₀₀₀ was used to prepare liposomes, and then, the grafting efficiency was further assessed. Figure 1G showed that liposomes with more hydrophilic surfaces exhibited significantly higher fluorescence intensity, which was consistent with the increase in color intensity observed in the liposome suspensions (Figure S1). Quantitative analysis using a microplate reader (Figure 1H) confirmed that the DSPE-PEG content was consistent with the feeding ratio of lipid to DSPE-PEG₂₀₀₀.

To assess the success of the hydrophilicity modulation, water contact angle measurements were conducted. Theoretically, a contact angle greater than 90° suggests that the tested surface is hydrophobic.⁴¹ As shown in Figure 1I, the contact angle decreased progressively from $57.6 \pm 0.8^{\circ}$ for LH Lip to $35.5 \pm 0.3^{\circ}$ for MH Lip and $25.8 \pm 2.1^{\circ}$ for HH Lip, demonstrating a clear trend in surface hydrophilicity corresponding to the DSPE-PEG₂₀₀₀ content. In other words, LH Lip was slightly hydrophobic among these liposomes. Besides, the Coomassie brilliant blue (CBB) method was applied to measure the hydrophobic surface property of liposomes.²⁵ CBB is a hydrophobic dye that shifts from red $(\lambda_{\text{max}} = 488 \text{ nm})$ to blue upon binding to hydrophobic surfaces, with the higher redshift magnitude ($\Delta\lambda$ values) correlating to higher hydrophobicity. As shown in Figure 1J, $\Delta\lambda$ values increased as the PEG content decreased, indicating a corresponding increase in the surface hydrophobicity of the liposome. This trend aligned with the contact angle measurements, confirming the successful fabrication of liposomes with distinct surface hydrophilicity.

Notably, it was quite essential for nanovehicles to keep colloidal stability after aerosolizing and in the lung fluid. Initially, a microsprayer aerosolizer was used to collect liposome suspensions after atomization, which could provide quantitative aerosol delivery for small animals. 42-44 All the

nebulized liposome suspensions displayed uniform aerodynamic diameter distribution with a homogeneous and fine spray (Figure S2A,B). We compared the DLS diameters of liposomes before and after aerosolization. The results of Figure 1K showed that aerosolization did not induce size variation, suggesting that the liposomes retained their structural integrity during aerosol delivery. Förster resonance energy transfer (FRET) assays, using FITC-labeled DSPE-PEG₂₀₀₀ and DiI as fluorescent probes, further verified the preservation of liposome integrity postaerosolization and during the pulmonary delivery process in mouse-extracted bronchoalveolar lavage fluid (BALF) (Figures S3 and 1L). Besides, the DLS size of all liposomes incubated in BALF remained stable within the 12 h incubation period (Figure 1M), underscoring the robustness of these formulations in lung fluid.

In conclusion, we successfully prepared liposomes with tunable surface hydrophilicity by varying the lipid-to-DSPE-PE G_{2000} ratio. These liposomes exhibited identical size, surface charge, rigidity, and good stability under conditions mimicking aerosol delivery and pulmonary environments.

2.2. Surface Hydrophilicity Regulation Governs the In Vivo Distribution of Inhaled Liposomes. The impact of surface hydrophilicity/hydrophobicity on the absorption and distribution of inhaled liposomes was explored. Mice were aerosolized with liposome suspensions dispersed in sterile saline solution via a microsprayer aerosolizer under anaesthetized conditions (Figure 2A). First, male mice were administered with coumarin-6 (C6) loaded liposomes, and blood samples were collected at different time intervals postinhalation. The fluorescence intensity of C6 in the blood was then measured. The blood concentration-time profiles (Figure 2B) revealed that liposomes with less hydrophilicity achieved significantly higher blood concentrations than their highly hydrophilic counterparts, even at 24 h postinhalation. This suggests that LH Lip was prone to penetrate across the alveolar epithelium. These findings were further corroborated by the area under the curve (AUC) (Figure 2C), which showed a clear trend of enhanced absorption for lower hydrophilic (slightly hydrophobic) formulations.

To further investigate the in vivo distribution of inhaled liposomes, we used an in vivo imaging system (IVIS) to track the transportation of liposomes labeled with DiD (1,1'-Dioctadecyl-3,3,3',3'- Tetramethylindodicarbocyanine, 4chlorobenzenesulfonate Salt) in the lungs over time. As shown in Figure 2D, free DiD dye was rapidly eliminated from the lungs, with fluorescence signals becoming undetectable by 6 h. In contrast, liposome formulations exhibited prolonged retention in the lungs, with DiD signals detectable for up to 24 h. Interestingly, the rate of DiD elimination from the lungs accelerated with the increase of surface hydrophobicity. At 24 h, fluorescence signals from the MH Lip and LH Lip groups were barely monitored. In contrast, HH Lip showed the strongest and most sustained fluorescence accumulation in the lungs, which remained detectable up to 48 h. Semiquantitative region-of-interest (ROI) analysis (Figure 2E) further supported these observations.

Following in vivo imaging, mice were sacrificed, and their lungs (Figure 2F,G) were harvested for ex vivo analysis, as well as the extra-pulmonary organs (Figure S4A,B). Free dye was entirely cleared from both the lungs and other organs due to its rapid metabolism. LH Lip, with relatively low pulmonary retention, showed significantly higher distributions in the liver, spleen, and kidney. In contrast, HH Lip maintained a high level

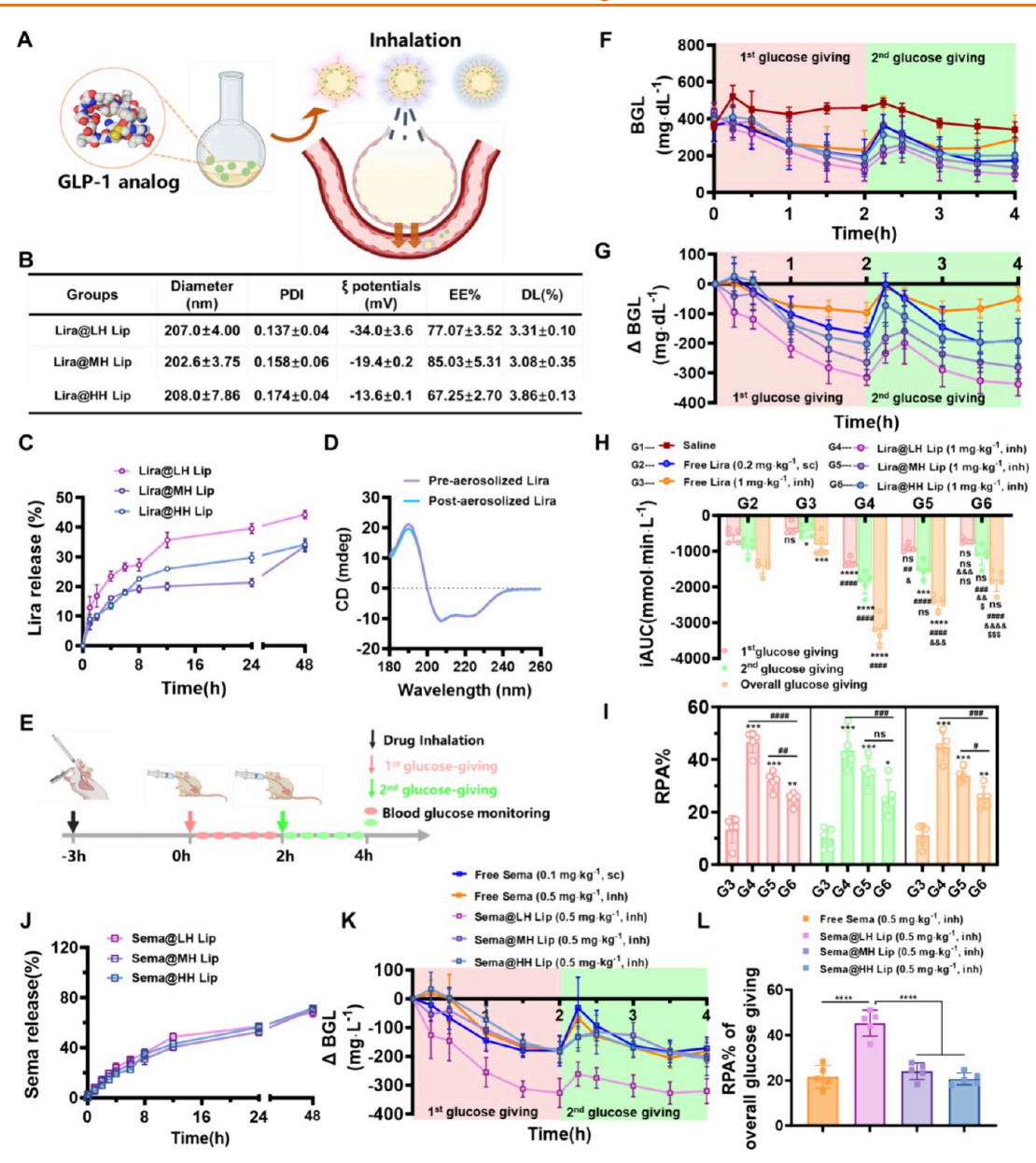


Figure 3. GLP-1 agonists loaded low hydrophilic liposome has better hypoglycemic effect than high hydrophilic liposome. (A) Illustration of GLP-1 RAs loaded liposomes with different surface hydrophilicity after inhalation, including drug encapsulation of GLP-1 RAs, the process of inhalation, and absorption into blood circulation. (B) Characterizations of liposomes with different surface hydrophilicity encapsulating Lira, n = 3. (C) In vitro release behavior of Lira@Lip with different surface hydrophilicity in simulated lung physiological media, PBS (pH 7.4), n = 3. (D) Circular dichroism spectroscopy characterization of Lira before and after atomization. (E) Schematic illustration of the oral glucose tolerance test (OGTT) process. T2DM KKAy mice that were fasted overnight and their fasting blood glucose (FBG) levels were assessed before treatment. Mice were aerosolized with saline (G1), Free Lira solution (1 mg·kg⁻¹, G3), Lira@LH Lip (1 mg·kg⁻¹, G4), Lira@ MH Lip (1 mg·kg⁻¹, G5), or Lira@HH Lip (1 mg·kg⁻¹, G6), and mice in G2 were subcutaneously injected with Free Lira solution (0.2 mg· kg⁻¹). Blood glucose was measured at 0, 15, 30, 60, 90, and 120 min after administration of oral glucose solutions (0.2 g.kg⁻¹). (F) Original blood glucose levels (BGL) of T2DM KKAy mice during the oral glucose tolerance test (OGTT) after inhalation with different Lira formulation, n = 5. (G) Increment of blood glucose levels by subtracting the FBG (Δ BGL) during OGTT after inhalation with different Lira formulation (n = 5). (H) Corresponding incremental area under the curve (iAUC) of mice during OGTT after inhalation with different Lira formulation, n = 5. (*, #, and \$) mean group versus to G2, G3, G4, and G5, respectively. (I) Relative pharmacological bioavailability (RPA) of Lira formulations, RPA = (iAUC_{Gx} /Lira dose_{Gx})/ (iAUC_{G2}/Lira dose_{G2}), n = 5. (*) means group versus G3, and (#) means comparison between groups. (J) In vitro release behavior of Sema@Lip with different surface hydrophobicity in simulated lung physiological media, PBS (pH 7.4), n = 3. (K) The increment of BGL was by subtracting the FBG (Δ BGL) during OGTT. Mice were administrated with inhalation of free Sema, Sema@LH Lip, Sema@MH Lip, and Sema@HH Lip (0.5 mg kg⁻¹), subcutaneous injection of free Sema (0.1 mg kg⁻¹) (n = 5). (L) Relative pharmacological bioavailability (RPA) of Sema formulations during the overall glucose giving period, RPA = (iAUC_{Gx} /Sema dose_{Gx})/ (iAUC_{G2}/Sema dose_{G2}), n = 5. (*) means group versus Sema@LH Lip. [Data are presented as mean ± SD. Statistical significance was calculated via one-way ANOVA, followed by Tukey's multiple comparison. (*, #, &, \$) P < 0.05, (**, ##, &&, \$\$) P < 0.01, (***, ###, &&&, \$\$\$) P < 0.001]. Labels (A) and (E) were created using https://www.biorender.com with a license agreement.

of retention in the lung, with minimal fluorescence observed in other organs.

To investigate the pulmonary distribution of liposomes, we further analyzed the residual fluorescence intensity in BALF collected from mice at 0, 24, and 48 h postinhalation of DiI@ Lips. As shown in Figure 2H, mice treated with the HH Lip had significantly higher fluorescence in BALF, suggesting a greater retention in the pulmonary cavity rather than inside the cells. To visualize liposome localization, lung sections at 24 and 48 h postinhalation were stained with FITC-WGA to label the surface mucus. Most HH Lip accumulated in the alveolar region, consistent with its low systemic absorption efficiency (Figure 2I). Notably, in the bronchial region, HH Lip was observed between the mucus layer and the epithelial cells (as indicated by white arrows). Previous studies have shown that bronchial mucus consists of two distinct layers: an outer gellike layer that primarily serves as a barrier against foreign particles and an inner aqueous layer that facilitates ciliary movement. Based on this, we hypothesized that HH Lip accumulated in the aqueous mucus layer, shielded by the outer mucus layer in the bronchial region, further confirming its prolonged retention in the lungs.

Taken together, our results highlight the critical influence of surface hydrophilicity on the biodistribution of inhaled liposomes. Highly hydrophilic liposomes preferentially accumulate in the lung, while slightly hydrophobic ones are more prone to translocate into the bloodstream. Therefore, we further investigated the therapeutic effects of different drugs after loading them into these liposomes.

2.3. Low Hydrophilic Liposome Loaded with GLP-1 Agonists Generate Superior Hypoglycemic Effects Compared to High Hydrophilic Liposomes. Encouraged by the enhanced absorption performance of slightly hydrophobic liposomes after inhalation, we further evaluated the in vivo therapeutic efficacy of loaded drugs for systemic delivery. Glucagon-like peptide-1 receptor agonists (GLP-1 RAs) have gained significant attention for their exceptional ability to regulate blood glucose and maintain body weight. 45,46 Among these, liraglutide (Lira) and semaglutide (Sema) are widely recognized as leading therapeutic agents. The commercial success of Rybelsus, the only oral GLP-1 RA product currently on the market, proves the charming appeal of mucosal delivery. 47 Pulmonary delivery, characterized by a larger absorptive surface area and a milder microenvironment compared to oral administration, has attracted considerable interest. In this study, Lira was selected as a model drug for the development of inhalable GLP-1 RA therapies.

Lira was encapsulated into liposomes using the above-described methods. As shown in Figure 3B, the particle size of Lira@Lip was consistent with that of blank liposomes (~200 nm) and exhibited good dispersion. All formulations achieved encapsulation efficiencies of 65–85% and drug loading efficiencies of 3.0–4.0%. Moreover, the encapsulation of Lira did not alter surface hydrophilicity among Lira@Lips (Figure SSA). In vitro drug release profiles in PBS (pH 7.4, Figure 3C) demonstrated a slow and sustained drug release over 48 h without a burst release. To assess the impact of aerosolization on the bioactivity of Lira, we utilized circular dichroism (CD) spectroscopy. The spectra revealed no significant changes in Lira's secondary structure postaerosolization (Figure 3D), indicating preservation of Lira's bioactivity.

Then, the near-infrared dye CyS-labeled Lira (Cy5-Lira) was encapsulated into liposomes with different surface hydro-

philicity to estimate the pharmacokinetic behaviors of drugloaded liposomes. All Cy5-Lira@Lips showed identical particle size and dispersion with Lira@Lips (Figure S6A). Of note, Cy5-Lira@LH Lip still possessed the highest systemic absorption (higher AUC and C_{max}) within 24 h in Figure S6B,C, with much faster elimination from lungs compared to Cy5-Lira@HH Lip (Figure S6D,E). Next, we performed oral glucose tolerance tests (OGTT) on type 2 diabetic mellitus (T2DM) KKAy mice to evaluate the antidiabetic efficacy and delivery efficiency of Lira@Lips with varying surface hydrophilicity (Figure 3E).⁴⁸ Following overnight fasting but free with water, mice received Lira@Lips via aerosolization for 3 h (at -3 h) prior to an oral glucose challenge (defined as 0 h). After a first glucose administration, blood glucose levels (BGL) were monitored for 2 h, then a second glucose challenge was performed to evaluate long-acting effects. Free Lira delivered via inhalation and subcutaneous injection served as controls. All treated mice initially exhibited hyperglycemia (fasting blood glucose ~400 mg·dL⁻¹), while saline-treated mice remained hyperglycemic throughout both testing periods (Figure 3F).

The ΔBGL (baseline-subtracted values) over 4 h were profiled in Figure 3G, and the incremental area under the curve (iAUC) values were provided in Figure 3H. Notably, all inhaled Lira formulations significantly reduced blood glucose levels compared to the controls. And Lira@Lip exhibited identical and even superior hypoglycemic effects compared to subcutaneous injection, likely due to the extensive absorptive surface area and rich blood flow in the pulmonary route. Among inhaled formulations, Lira@LH Lip achieved the strongest and most sustained glucose-lowering effects, even returning blood glucose levels to normal (~100 mg·dL⁻¹) after a single administration. The relative pharmacological bioavailability (RPA) of Lira@LH Lip, calculated as the ratio of inhaled iAUC to subcutaneous iAUC, reached 45%, further confirming the advantages of LH Lip (Figure 3I).

For further verification, we conducted parallel studies using another GLP-1 RAs, Sema. Characterization data for Semaloaded liposomes (Sema@Lip), surface hydrophilicity assay, and CD spectroscopy of aerosolized Sema were separately detailed in the Supporting Information (Table S1, Figures S5B, and S7), with release profiles shown in Figure 3J. Sema exhibited faster release compared to Lira, probably due to their structural differences. At half of the Lira dose, Sema@Lip also demonstrated potent glucose-lowering effects, with LH Lip showing the greatest efficacy (Figures 3K and S8). Interestingly, the performance of Sema@Lip differed substantially from that of Lira@Lip. Specifically, free Sema exhibited comparable hypoglycemic effects to Sema@HH Lip and Sema@MH Lip (Figure 3L), demonstrating that the surface hydrophilicity of liposome played a less important role in Sema compared with Lira, probably due to the longer hydrophobic fatty acid chains of Sema. 49 This reminds us that we should consider not only the properties of carriers but also those of the drug during the formulation design. Further exploration of drug-platform interactions is necessary to optimize inhalable nanodelivery systems for systemic therapy.

Pulmonary administration has long been regarded as an ideal route for systemic drug delivery, but efforts to commercialize inhalable systems have encountered some challenges. During the last 20 years, the development of inhalable delivery systems for systemic absorption had come to a standstill. So, S1 Recent advancements in nanotechnology, coupled with heightened

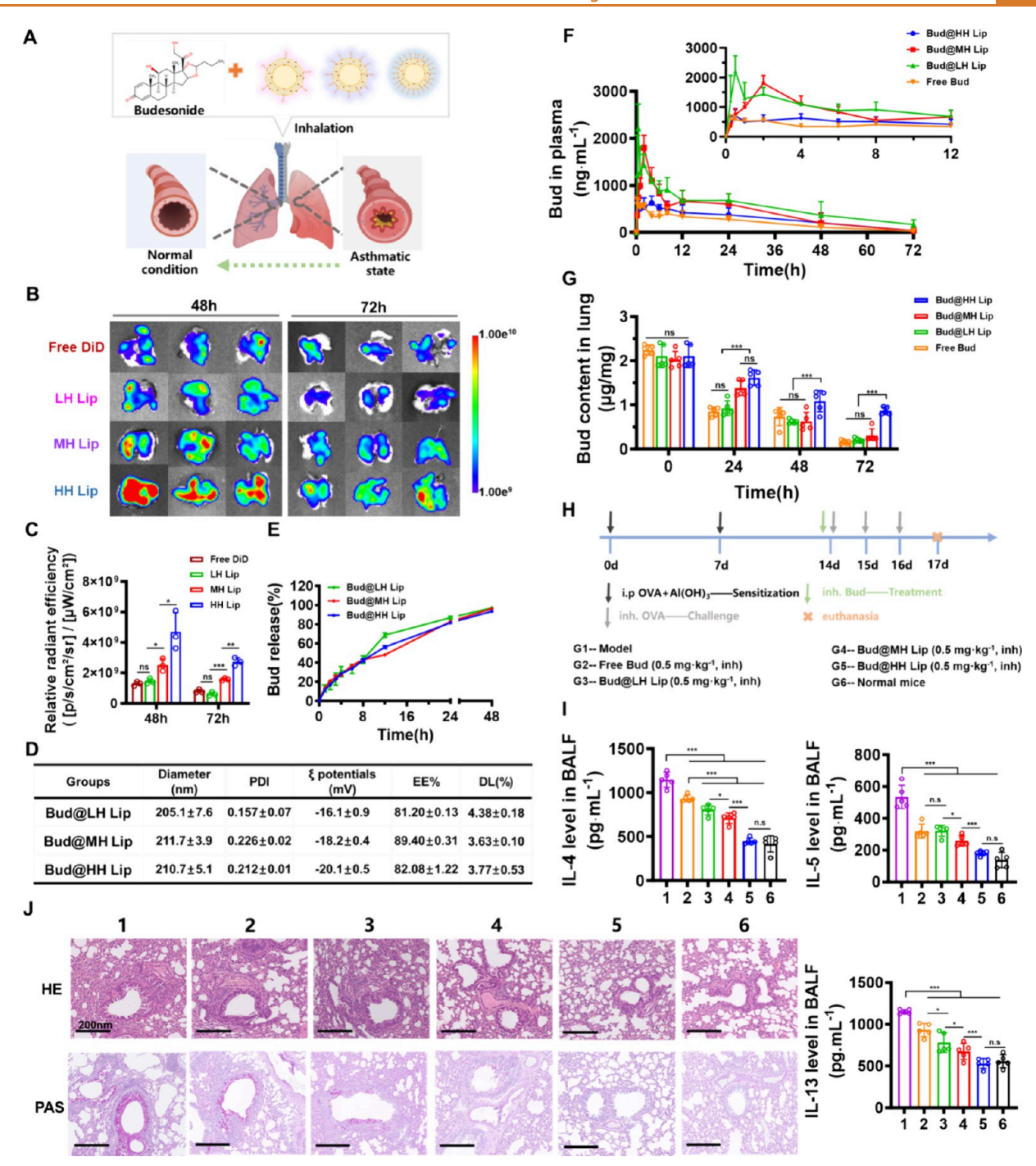


Figure 4. High hydrophilic liposome produced stronger lung retention capability and better efficacy of budesonide against acute asthma. (A) Illustration of lung tissue recovery from asthmatic state to normal condition, after inhalation of budesonide (Bud)-loaded liposomes in an OVA-induced acute asthma mouse model. (B, C) IVIS imaging and quantitative region-of-interest (ROI) analysis showing the distribution of inhaled DiD-labeled LH Lip, MH Lip, HH Lip and free DiD in OVA-induced acute asthma mice at 48 and 72 h, n = 3. (D) Characterization of budesonide (Bud)-loaded liposomes with different surface hydrophilicity, n = 3. (E) Release profiles of Bud from liposomes with different surface hydrophilicity in simulated lung physiological media for 48 h, PBS (pH 7.4), n = 3. (F) Plasma concentration profiles of Bud@LH Lip, Bud@MH Lip, Bud@MH Lip, Bud@HH Lip, and Free Bud in OVA-induced acute asthma mice, n = 5. (G) Budesonide content in lungs after 0 h, 24 h, 48 and 72 h inhalation with Bud@LH Lip, Bud@MH Lip, Bud@HH Lip, and Free Bud in OVA-induced acute asthma mice, n = 5. (**) means comparison between groups, (ns) means no significance. (H) Schematic representation of the experimental design about the Bud treatment in OVA-induced acute asthma mouse models. Asthmatic mice were administrated with inhalation of saline (G1), free Bud suspension (G2), Bud@LH Lip (G3), Bud@MH Lip (G4), or Bud@HH Lip (G5), and normal mice were treated with saline (G6). (I) Expression levels of inflammatory cytokines IL-4, IL-5, and IL-13 in BALF, n = 5. (J) Hematoxylin-eosin (HE) staining and periodic acid-Schiff (PAS) staining of lung tissues sections from OVA-induced acute asthma mice at end points. [Data are presented as mean \pm SD. Statistical significance was calculated via one-way ANOVA, followed by Tukey's multiple comparison. (*) P < 0.05, (**) P < 0.01, (***) P < 0.0

interest in respiratory therapies during the COVID-19 pandemic, have revitalized research in this area. Our findings also demonstrated the potential of inhalable nanodelivery systems for systemic drug delivery. Moreover, the slight augmentation of surface hydrophobicity on nanovehicles could immensely promote pulmonary absorption of GLP-1 RAs, which might indicate a promising therapeutic application.

2.4. High Hydrophilic Liposomes Exhibit Superior Lung Retention and Enhance the Therapeutic Efficacy of Budesonide in Acute Asthma. Our above-mentioned findings revealed that liposomes with higher surface hydrophilicity dramatically extended their retention time in the lung. This led us to hypothesize that such characteristics might confer HH Lip with enhanced therapeutic effects for pulmonary diseases postinhalation, while also minimizing systemic drug toxicity. To verify this hypothesis, we evaluated their performance in a mouse model of ovalbumin (OVA)-induced acute allergic asthma, one of the commonest respiratory disorders (Figure 4A). 52

First, the asthma model was successfully established, as evidenced by bronchial wall thickening, excessive mucus secretion (Figure 4J), and elevated cytokine levels of IL-4, IL-5, and IL-13 compared to normal mice (Figure 4K). S3,54 Considering that pathological changes in asthmatic lungs may influence liposome absorption, we reassessed the pulmonary distribution of liposomes with varying surface hydrophilicity in the asthma model, and free DiD was served as control (Figure 4B,C). Notably, HH Lip maintained the strongest fluorescence signals for up to 72 h, consistent with their performance in healthy mice (Figure 2F). All liposome formulations, even free DiD, exhibited slower clearance rates in asthmatic lungs, likely due to the altered pulmonary microenvironment.

Next, budesonide (Bud), a first-line glucocorticoid for asthma treatment, was encapsulated into the liposomes.³⁵ Budesonide was well-recognized for its potent anti-inflammatory and antiasthmatic properties, yet its clinical application was often hindered by rapid clearance and frequent dosing requirements. The physicochemical properties of the Budloaded liposomes were characterized (Figure 4D), showing uniform particle sizes (~200 nm) and high encapsulation efficiencies (>80%). And Bud@Lips displayed distinct differences in surface hydrophilicity as well (Figure S9). In vitro release studies revealed a sustained release profile over 48 h in PBS (pH 7.4, Figure 4E). Likewise, a pharmacokinetic study of Bud@Lips following inhalation was conducted. Specifically, the acute allergic asthma mice were aerosolized with Free Bud, Bud@LH Lip, Bud@MH Lip, and Bud@HH Lip (Bud: 2 mg· kg⁻¹), respectively. Blood samples were collected at different time intervals within 72 h and were centrifuged (3500 rpm, 4 °C, 5 min) to obtain plasma for further analysis. Then, Bud in plasma was detected by HPLC after a series of extraction processes according to previous reports. The corresponding plasma concentration-time curves and pharmacokinetic parameters were obtained (Figure 4F and Table S2). Consistent with the pharmacokinetic results of the fluorescently labeled liposomes, Bud@HH Lip exhibited significantly reduced systemic exposure compared with Bud@MH Lip and Bud@HH Lip. As the major therapeutic site of inhaled Bud, lung tissues were harvested and Bud contents were further quantified at 0, 24, 48, and 72 h postinhalation (Figure 4G). Notably, Bud@HH Lip showed highly enhanced pulmonary retention all the time.

We then assessed the therapeutic efficacy of Bud@Lip in an acute asthma model according to the protocol outlined in Figure 4H. Previous studies have shown the improved therapeutic efficacy of liposome-encapsulated Bud with daily administration in acute asthma models.⁵⁵ Based on the aforementioned prolonged retention of Bud@HH Lip, we hypothesized that it might achieve similar therapeutic outcomes with a single administration. Following OVA sensitization and intranasal challenges, Bud formulations were aerosolized, and asthma-related indices were subsequently determined and analyzed. Bud@HH Lip demonstrated the most pronounced downregulation of inflammatory cytokines IL-4, IL-5, and IL-13 in bronchoalveolar lavage fluid (BALF), with levels returning to those of normal mice (Figure 4I). Furthermore, histological analysis via HE and PAS staining (Figure 4J) revealed that untreated asthma mice exhibited severe pathological changes, including bronchial wall thickening, parenchymal alterations, and excessive mucus secretion. These symptoms were slightly alleviated in free Bud, Bud@LH Lip, and Bud@MH Lip treated groups. Encouragingly, Bud@ HH Lip nearly restored lung histology to a normal state, demonstrating superior therapeutic efficacy.

Pulmonary drug delivery offered multiple advantages for respiratory diseases, including higher local drug concentrations and faster onset of action. However, challenges, such as rapid drug clearance and systemic exposure, persist. Several research studies suggested that surface hydrophilicity/hydrophobicity may influence the residence of inhaled NPs in the lung. Kaminskas et al. reported that polymeric nanoparticles conjugated with hydrophobic drug methotrexate (MTX) exhibited a significantly faster pulmonary clearance than unmodified nanoparticles.²⁹ In contrast, another report demonstrated that PEG-modified nanoparticles with enhanced mucus penetration prolonged lung retention by reducing macrophage uptake. 56 On the basis of previous studies about the employment of inhaled liposomes in delivering Bud, we further achieved effectively prolonged lung retention and enhanced antiasthmatic efficacy with reduced dosing frequency by means of surface hydrophilicity modulation of liposomes. This strategy holds promise for improving treatment outcomes, patient compliance, and overall respiratory health in the management of local pulmonary diseases.

Moreover, due to the involvement of three types of liposomes with varying surface hydrophilicity and three drugs with distinct physicochemical properties, notable associations between the drugs and their respective carriers were identified. Based on the structural characteristics of the liposomes and the mechanisms of drug loading, hydrophobic small molecules (e.g., budesonide) were primarily localized within the phospholipid bilayer, resulting in high encapsulation efficiency (81–90%). In contrast, peptides and proteins, which possess both hydrophilic and hydrophobic regions, exhibited different interactions depending on their overall hydrophilicity. Molecules with stronger hydrophilicity favored encapsulation within the aqueous core, while those with greater hydrophobicity were more likely to associate with the lipid bilayer. For instance, due to its longer fatty acid side chain, Sema may exhibit stronger interactions with the bilayer, whereas Lira appears to be more localized within the aqueous core. Nevertheless, both peptides demonstrated comparable encapsulation efficiencies (65-70%). Differences in release profiles were also observed among the three drugs. Lira, predominantly associated with the aqueous core, exhibited the slowest release

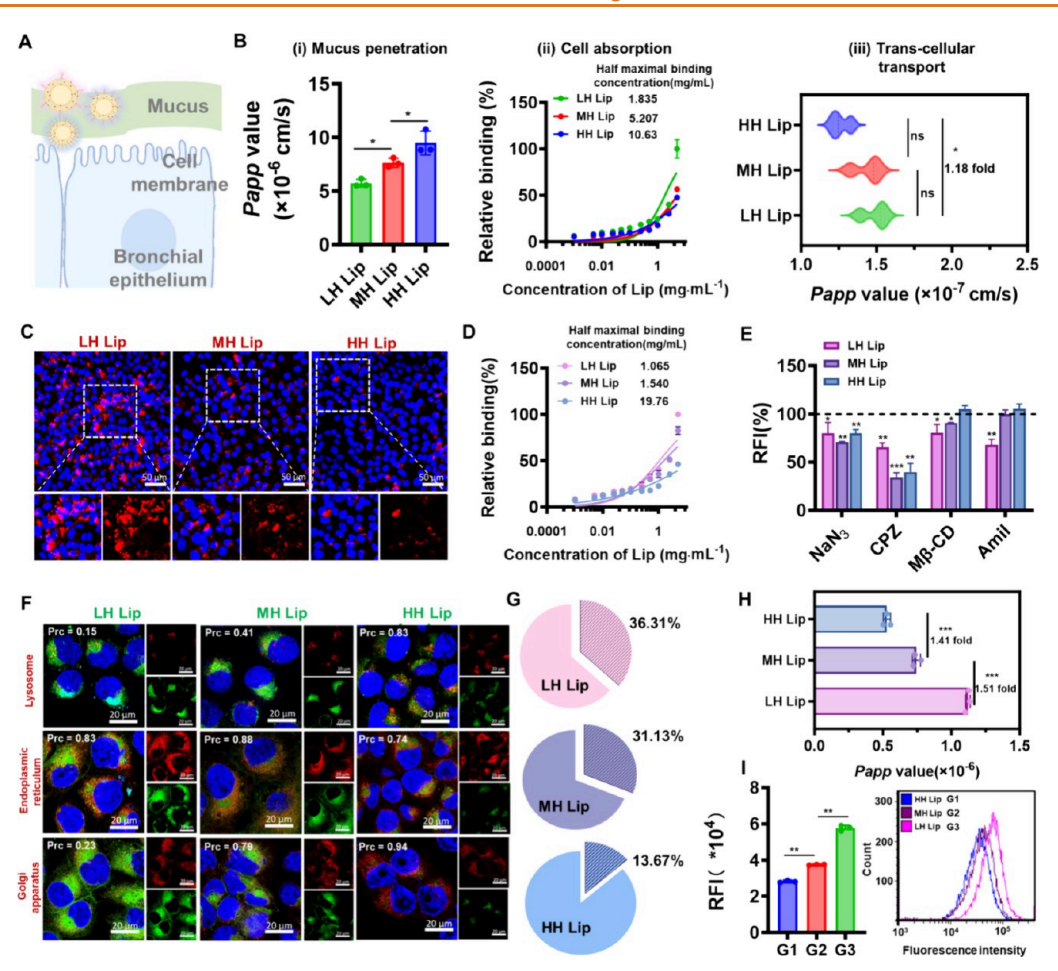


Figure 5. Liposomes with variable hydrophilicity exhibit various behaviors toward different pulmonary cells. (A) Illustration about transport process of liposomes with different hydrophilicity on bronchial epithelial cells. (B) Investigations about transport process of liposomes with different hydrophilicity on bronchial epithelial cells, including (i) apparent permeability coefficients (P_{app}) of liposomes with different hydrophobicity on 3D transwell chambers constructed simulated bronchial mucus setup; (ii) Cell binding rate of liposomes with Calu-3 cell under 4 °C for membrane affinity measurement. The liposome concentration-binding rate curves and the half maximal binding concentration were fitted and calculated by Graphpad, n = 3; (iii) Apparent permeability coefficients ($P_{\rm app}$) of liposomes with different hydrophobicity across Calu-3 monolayer epithelial cells, n = 3. (C) Representative confocal microscopy images showing cellular internalization of liposomes with different hydrophobicity in NCI-H441 Cells, scale bar = 50 µm. Legend: blue, cell nuclei; red, DiI-labeled liposomes. (D) Cell binding rate of liposomes with NCI-H441 cells under 4 °C for membrane affinity measurement. The liposome concentration-binding rate curves and the half maximal binding concentration were fitted and calculated by Graphpad, n = 3. (E) Investigation of cellular uptake pathways of liposomes using various endocytosis-blocking inhibitors, including NaN3 for energy-blocking, CPZ (Chlorpromazine) for blocking clathrin-mediated endocytosis, β -CD for blocking caveolin-mediated endocytosis and Amil (amiloride) for blocking micropinocytosis route, (*) means group versus to cells without incubation with chemical inhibitors, n = 5. (F) Representative confocal microscopy images showing the colocalization of liposomes with intracellular organelles, including lysosomes, ER, and golgi apparatus in NCI-H441 Cells, the Pearson coefficient (Prc) was calculated by ImageJ; scale bar = 20 µm. Legend: blue, cell nuclei, red, organelles, green, DiI-labeled liposomes. (G) Average exocytosis rates of liposomes with different hydrophobicity on NCI-H441 Cells, n = 3. (H) Apparent permeability coefficients ($P_{\rm app}$) of liposomes with different hydrophobicity across NCI-H441 monolayer epithelial cells, n=3. (I) Cellular uptake of HH Lip (G1), MH Lip (G2), and LH Lip (G3) in macrophages via flow cytometry. n = 3. [Data are presented as mean ± SD. Statistical significance was calculated via one-way ANOVA, followed by Tukey's multiple comparison. (*) P < 0.05, (**) P < 0.01, (***) P < 0.001.] Label (A) was created using https:/www.biorender.com with a license agreement.

(<40% at 48 h), followed by the more hydrophobic Sema (<70% at 48 h). Budesonide (Bud), residing within the bilayer, was released most rapidly (nearly 100% at 48 h). These differences in release kinetics had a direct effect on in vivo delivery. Specifically, Lira@LH Lip, characterized by a slower release profile, had improved bioavailability compared to Sema@LH Lip.

Interestingly, the surface hydrophilicity of the liposomes appeared to have minimal influence on drug encapsulation efficiency. However, in terms of release behavior, Lira@LH Lip showed a slightly faster release rate compared to those of

Lira@MH Lip and Lira@HH Lip, possibly owing to the increased steric hindrance imposed by the hydrophilic surface components on the hydrophilic macromolecule Lira. In contrast, no significant differences in release behavior were observed among the three liposomal formulations for the other two drugs.

Thus, these results emphasize that a thorough understanding of drug—carrier interactions is essential for the rational design of liposomal nanocarriers, as such interactions profoundly influence encapsulation efficiency, release behavior, and in vivo bioavailability, ultimately shaping the therapeutic outcomes.

2.5. Liposomes with Variable Hydrophilicity Exhibit Various Behaviors toward Different Pulmonary Cells.

Our findings revealed intriguing differences in the biodistribution patterns of liposomes with different surface hydrophilicity. To uncover the underlying mechanisms, we systematically investigated the performance of liposomes in their transport to the lungs.

The lung is anatomically divided into the conducting airways and alveolar regions. Conducting airways are primarily related to ciliated and secretory epithelial cells, overlaid by a duallayered mucus blanket (Figure 5A).⁵⁷ The particles trapped in mucus would be cleared out to the oropharynx through the mucociliary system. Therefore, we endeavor to unravel the interactions of the liposomes deposited on the conducting airway stage by stage (Figure 5B). First, although HH Lip exhibited the best mucus-penetrating ability among the three liposomes in the 3D transwell chamber, which was consistent with previous studies, they showed weaker membrane affinity with Calu-3 cells, an in vitro bronchial epithelial cells.⁵ Therefore, HH Lip finally possessed inferior transcellular transport ability in Calu-3 monolayer epithelial cells compared with that of LH Lip. Of note, the mucus barrier might narrow the difference of Papp values through bronchial epithelium between HH Lip and LH Lip, and the modulation strategies catering to transcellular barriers (lower hydrophilicity) seem to be more decisive for the better trans-epithelial absorption of NPs.^{37,59} However, HH Lip, owing to the antifouling ability provided by enhanced surface hydrophilicity, which exhibited limited cellular uptake, might be better suited for sustaining drug retention and therapeutic effects in the local pulmonary environment under the specific shielding effect of bronchial mucus.

Since the surfactants covering alveolar epithelial cells were just a thin layer, and concerning investigations about the intracellular transport of NPs across alveolar epithelium were limited, we focused our attention mainly on the interplays of liposomes and alveolar epithelium. NCI-H441, the first cell line of human distal lung epithelial origin with nearly similar characteristics as primary alveolar epithelia, was selected as a cell model for the following in vitro evaluation. 60,61 As expected, the cellular uptake of liposomes gradually decreased with the augmentation of surface hydrophilicity in the confocal images in Figure 5C. The cell binding affinity of liposomes to NCI-H441 cells exhibited a significant negative correlation with surface hydrophilicity, which could be attributable to the weakened hydrophobic interactions with the cell membrane (Figure 5D). In addition, the cellular uptake of all liposomes had a significant decline after NaN3 and chlorpromazine (CPZ) treatment, implying the involvement of energydependent endocytosis and the clathrin-mediated (CME) pathway (Figure 5E). Interestingly, caveolae-mediated endocytosis (CvME) and macropinocytosis routes also participated in the internalization of LH Lip, which greatly amplified the endocytosis efficiency.⁶²

We further investigated the intracellular trafficking of liposomes by using CLSM (Figure 5F). HH Lip showed uniform distribution across the endoplasmic reticulum (ER), Golgi apparatus, and lysosomes, with the Pearson coefficient (Prc) of 0.74, 0.94, and 0.83, respectively. In contrast, LH Lip (slightly hydrophobic liposomes) exhibited a distinct trafficking pattern characterized by limited lysosomal colocalization (coefficient of 0.15) and preferential accumulation in the ER (coefficient of 0.83). This divergence in trafficking can be

attributed to the involvement of the CvME pathway, which likely facilitated the bypassing of the lysosomal degradation route and directed the liposomes toward secretory organelles such as the ER. Likewise, the exocytosis rate of liposomes using relevant inhibitors on NCI-H441 cells also showed that the exocytosis of LH Lip was greatly dependent on the ER-golgirelated pathway, with the avoidance of the endolysosome pathway. (Figure S11). As shown in Figure 5G, LH exhibited significantly higher exocytosis rates (36.31%) compared to those of MH Lip (31.13%) and HH Lip (13.67%). To mimic the pulmonary alveolar epithelial barrier, we constructed a 3D transwell model using NCI-H441 cells with transepithelial electrical resistance (TEER) values exceeding 600 $\Omega \cdot \text{cm}^2$ and overexpressed tight junction structure (Figure S10). Consequently, LH Lip showed the highest apparent permeability coefficient ($P_{\rm app}$), which was 1.51-fold and 2.2-fold higher than that of MH Lip and HH Lip, respectively (Figure 5H). Additionally, lung macrophages engaged in the phagocytosis of microorganisms and particulates. Therefore, we investigated the pinocytosis of macrophages toward our prepared liposomes. Figure 5I shows that macrophages preferentially phagocytize hydrophobic liposomes over hydrophilic liposomes. In other words, HH Lip was more likely to evade the clearance of macrophages and generate more durable residence.

In fact, the importance of surface hydrophobicity in enhancing trans-epithelial efficiency was previously investigated in our studies on intestinal mucosal epithelium. We found that the surface hydrophobicity of poly(lactic-co-glycolic acid) (PLGA) NPs influenced their exocytosis behaviors without affecting intracellular trafficking in intestinal epithelial cells. ²⁴ It seemed that surface hydrophobicity influenced not only the exocytosis of liposomes but also their transportation through the alveolar epithelial cells.

In summary, we propose a comprehensive hypothesis regarding the distinct distribution and absorption behaviors of hydrophilic and hydrophobic liposomes. Using an atomization device, all liposomes achieved a similar deposition on the alveolar and bronchial surfaces. On the bronchial surface, with the presence of a mucus barrier, higher hydrophilic liposomes demonstrated superior mucus penetration but limited transcellular transport compared to slightly hydrophobic liposomes, which might indicate the importance of a balance between surface hydrophilicity and hydrophobicity. In the alveolar region, the thin surfactant layer covering on alveolar epithelial cells was not enough to impede the passage of the liposomes. Of note, lower hydrophilic liposomes, with enhanced membrane avidity, multiple endocytosis pathways, and lysosome-bypassing transport, exhibited superior transepithelial absorption and systemic distribution compared with HH Lip. Thereby, the inhaled liposomes with different hydrophilicity lead to distinct in vivo distribution and therapeutic effects. Meanwhile, pulmonary macrophages also preferentially take up LH Lip compared to HH Lip, which accelerates the clearance of LH Lip while promoting prolonged retention of HH Lip in the lungs. This would be beneficial for hydrophilic nanoplatforms for their local drug delivery in the lungs. These findings stress the importance of tailoring NPs' surface properties to optimize therapeutic outcomes based on the intended site of action.

2.6. Inhaled Liposome with Variable Hydrophilicity Had Good In Vitro and In Vivo Biocompatibility. The emergence of nanotechnology in recent decades has

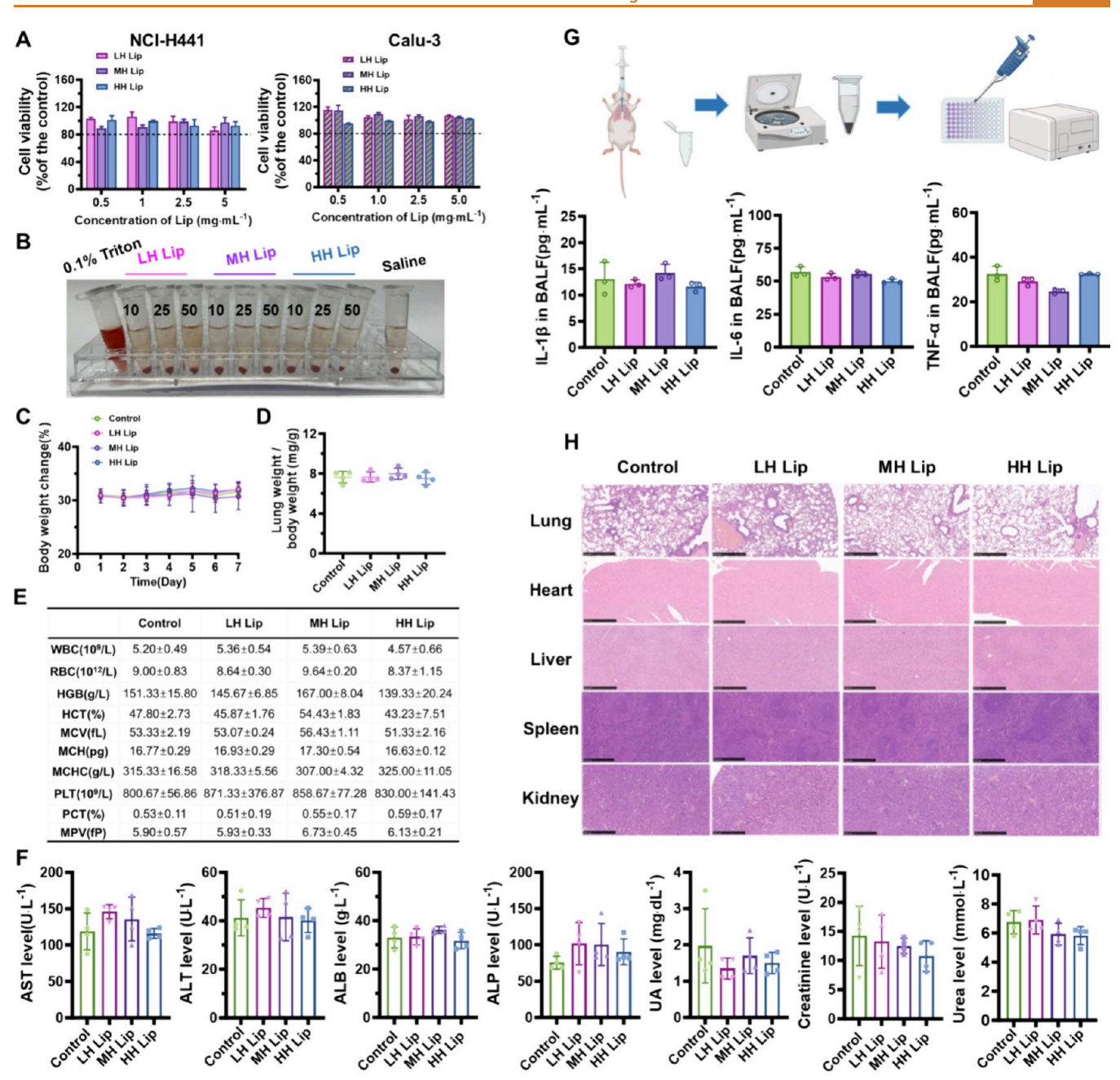


Figure 6. Inhaled liposome with variable hydrophilicity had good in vitro and in vivo biocompatibility. (A) Cellular viability study of alveolar epithelial NCI-H441 cells and bronchial epithelial Calu-3 Cells after 3 h of incubation of liposomes, n = 5. (B) Physical images showing hemolysis of red blood cells after 3 h-incubation of liposomes, n = 3. (C) Body weight change of ICR mice within 7 d after twice inhalation of blank liposomes (LH Lip, MH Lip or HH Lip) or saline solution, n = 5. (D) Ratio of lung weight to body weight at the end points. (E) Summary sheet of blood routine index in ICR mice after twice inhalation of liposomes or saline solution. (F) Expression levels of liver -related (AST, ALT, ALB, ALP) and kidney-related (UA, Creatinine, Urea) functional enzymes in the blood at the end points. (G) Expression levels of inflammatory cytokines in BALF of mice, including IL-1 β , IL-6, and TNF- α . (H) Hematoxylin-eosin (HE) staining of lung, heart, liver, spleen, and kidneys tissues sections from mice at end points. [Data are presented as mean \pm SD. Statistical significance was calculated via one-way ANOVA, followed by Tukey's multiple comparison. (*) P < 0.05, (**) P < 0.01, (***) P < 0.001.] Figure 6G was partly created using https://www.biorender.com with a license agreement.

significantly influenced the pharmaceutical industry, offering new approaches to drug delivery. However, concerns about the biosafety and potential toxicity of nanomaterials have garnered significant attention. Various evaluation methods and standards have been established alongside a growing body of research on these materials. Although we deliberately selected the liposomes as nanocarriers due to their favorable biocompatibility. While hydrophobic materials demonstrating strong bioaffinity with cell membranes compelled us to worry about the possibilities of biological membranes disruption. ^{63,64}

Pulmonary delivery has received great interest because of notable advantages in these years. However, the inhaled delivery systems should be safe enough not to hamper the normal respiratory functionalities of the lungs. Besides, some reports indicate the potential systemic risks of inhaled particles for systemic exposure in extrapulmonary organs. 65,66 Although

the extent of exposure and mechanisms of systemic translocations remain controversial, it is crucial to conduct a thorough biosafety evaluation of inhalable liposomes with different hydrophilicity.

In our study, we systematically assessed the biocompatibility of liposomes with varying hydrophilicity. In vitro experiments revealed that liposomes did not affect the viability of NCI-H441 or Calu-3 cells at concentrations ranging from 0.5 to 5 mg·mL⁻¹ (Figure 6A), even for TC-1 cells, the normal lung cells (Figure S12). These findings suggested that the prepared liposomes, irrespective of their hydrophilicity or hydrophobicity, exhibit negligible cytotoxicity. Furthermore, incubation of the liposomes with red blood cells for 3 h did not induce hemolysis (Figure 6B), as confirmed by quantitative analysis (Figure S13). Compared with other hydrophobic particles known to impair membrane integrity, these liposomes appear to be much safer, underscoring their compatibility with biological membranes.

To evaluate in vivo safety, mice were exposed to two doses of liposomes via inhalation over a 7-day period, with saline-treated mice serving as controls. Results showed no significant differences in body weight gain between the liposome-treated and control groups (Figure 6C). Similarly, lung weight indices (Figure 6D), hematological parameters (Figure 6E), and liverand kidney-related biochemical markers (Figure 6F) showed no abnormalities. Importantly, no signs of toxicity were detected in other organs (Figure 6H), supporting the systemic safety of the prepared liposomes.

Additionally, inflammatory cytokine levels in BALF were measured, as shown in Figure 6G. Liposome-treated groups displayed no significant elevations in IL-1 β , IL-6, or TNF- α levels, which means no occurrence of inflammatory responses in lungs. In the histological analysis of lung tissue, no visible physiological damage was found in liposome-treated mice (Figure 6H).

Collectively, these findings demonstrate that inhalable liposomes with varying hydrophilicity possess good biocompatibility both locally in the lungs and systemically. This favorable safety profile makes them promising candidates for drug delivery applications. The results also highlight the importance of designing nanocarriers with optimized hydrophilicity/hydrophobicity to balance therapeutic efficacy and biosafety, providing a strong foundation for the further development of inhalable nanotherapeutics.

3. CONCLUSIONS

In summary, this work proposed an inhaled liposome-based drug delivery system for both effective systemic and local delivery by modulating surface hydrophilicity/hydrophobicity of nanocarriers and revealed underlying interactions between these liposomes and pulmonary epithelial cells. Upon inhalation, liposomes with various hydrophilicity exhibited distinct absorption behaviors: low hydrophilic liposomes possessed favorable trans-alveolar capability and further elicited efficient hypoglycemic effects in T2DM mice when encapsulated systemic delivered GLP-1 RAs (Liraglutide or Semaglutide), while high hydrophilic liposomes displayed prolonged retention in lungs and produced stronger therapeutic effects in asthmatic models, on the basis of reduced budesonide dosing frequency. More detailed mechanism studies showed that lower surface hydrophilicity facilitated transepithelium of liposomes during the endocytosis-transcellular trafficking-exocytosis process on alveolar

epithelial cells. Meanwhile, more effective retentions of HH Lip could be attributed to the evasion of macrophage phagocytosis. Moreover, the inhaled liposomes exhibited desirable biocompatibility for both lung tissues and systemic organs. This study highlights surface hydrophilicity/hydrophobicity as a key factor in the rational design of inhalable nanocarriers for both local treatment and systemic delivery, offering valuable insights for mucosal delivery strategies.

4. EXPERIMENTAL SECTION

4.1. Cell Lines and Animals. NCI-H441 cells (American Type Culture Collection, HTB-174), purchased from Zhejiang Meisen Cell Technology Company (Zhejiang, China), were cultured in RPMI-1640 medium containing 10% fetal bovine serum (FBS), 1% sodium pyruvate, 100 U/mL penicillin, and 100 μ g/mL streptomycin. For the culture of the NCI-H441 monolayer on the 3D transwell, the original medium was further supplemented with dexamethasone (200 nM) and insulin-transferrin-sodium selenite (ITS) supplement. Calu-3 cells and mouse mononuclear macrophage leukemia cells (RAW264.7 cells) were obtained from the Institute of Biochemistry and Cell Biology (Shanghai, China). Calu-3 and RAW264.7 cells were cultured in Dulbecco's Modified Eagle Medium/Nutrient Mixture F-12 (F12/ DMEM) and Dulbecco's modified eagle medium (DMEM), respectively, supplemented with 10% (v/v) FBS, 1% nonessential amino acid, 1% (v/v) penicillin, and 100 IU/mL streptomycin. TC-1 cells, purchased from Xiamen Immocell Biotechnology Company (Xiamen, China), were cultured in RPMI-1640 medium containing 10% fetal bovine serum (FBS), 100 U/mL penicillin, and 100 μ g/mL streptomycin. All cells were cultured at 37 °C under a 5% CO₂ atmosphere.

BALB/c mice (male, 6–8 weeks, SPF) were purchased from the Sipeifu Experimental Animal Company (Beijing, China). KKAy mice (male, 6–8 weeks old, SPF) were purchased from Beijing HFK Bioscience Company (Beijing, China). ICR mice (male, 6–8 weeks old, SPF) were purchased from Dashuo Experimental Animal Company (Chengdu, China). All animal experiments were approved by the Medical Ethics Committee of Sichuan University and were performed in the Animal Laboratory of West China School of Pharmacy at Sichuan University (accreditation number: SYXK-(Chuan)2018-113).

4.2. Reagents and Materials. The soybean phospholipid mixture (SPCm) was purchased from Taiwei Pharmaceutical Co. (Shandong, China). 1,2-distearoyl-sn-glycero-3-phosphoethanolamine-N-[methoxy(polyethylene glycol)-2000] (DSPE-PEG₂₀₀₀) was bought from Ponsure Biotechnology Co. (Shanghai, China). Semaglutide (Sema) was provided by Chengdu Giant Pharmaceutical Technology Co., Ltd. (Sichuan, China). And Liraglutide (Lira) was kindly presented by HEC Pharmaceutical (Guangdong, China). Cholesterol was purchased from Chengdu Xiya Chemical Co., Ltd. (Sichuan, China). Courmarin 6 and chlorpromazine were obtained from Sigma-Aldrich Corporation (St. Louis, MO, USA). Bicinchoninic acid (BCA) protein assay kit, Brefeldin A, Monensin, ER-Tracker Red, and Golgi-Tracker Red were acquired from Beyotime (Shanghai, China). F12/DMEM cell culture mediums, Hank's Balanced Salt Solution (HBSS), 1,1'-dioctadecyl-3,3,3',3'-tetramethylindocarbocyanine perchlorate (DiI), 3,3'-dioctadecyloxacarbocyanineperchlorate (DiO), 1,1'-dioctadecyl-3,3,3',3' tetramethylindodicarbocyanine, 4-chlorobenzenesulfonate salt (DiD), and Lyso-Tracker Red were purchased from Invitrogen (USA). RPMI 1640 and DMEM cell culture mediums were purchased from BasalMedia (Shanghai, China). Stock solutions of penicillin and streptomycin, and nonessential amino acids were purchased from Solarbio Science & Technology (Beijing, China). 4',6-diamidino-2-phenylindole (DAPI) were purchased from Abmole (M5106, USA). Interleukin-4 (IL-4), IL-5, and IL-13 enzyme-linked immunosorbent assay (ELISA) were purchased from Wuhan Fine Biotech Co., Ltd. (Hubei, China). TNF-α, IL-6, and IL-1 β ELISA were bought from Thermo Fisher Scientific (USA). All other chemical reagents in the study were analytical grade.

4.3. Preparation and Characterization of Liposomes with Different Surface Hydrophilicities. Liposomes were prepared using a modified thin-film hydration-extrusion method, and liposomes with varying surface hydrophilicity were obtained by adjusting the weight ratio of the soybean phospholipid mixture (SPCm) to DSPE-PEG₂₀₀₀. The feeding ratios of SPCm to DSPE-PEG₂₀₀₀ were set at 10:2, 10:4, and 10:8, corresponding to LH Lip, MH Lip, and HH Lip. Specifically, SPCm, cholesterol, and varying amounts of DSPE-PEG₂₀₀₀ were dissolved in chloroform. The solvent was then evaporated at 37 °C for 1 h to form a thin lipid film, which was subsequently hydrated with 4 mL of deionized water for 30 min. The hydrated lipid suspensions were extruded through a polycarbonate membrane (pore diameter: 0.4 μ m) for 9 passes to produce the final liposomes.

Fluorescently labeled liposomes were prepared by incorporating dyes such as coumarin-6 (C6), 1,1'-dioctadecyl-3,3,3',3'-tetramethy-lindocarbocyanine perchlorate (DiI), 3,3'-dioctadecyloxacarbocyanine perchlorate (DiO), or 1,1'-dioctadecyl-3,3,3',3'-tetramethylindodicarbocyanine, 4-chlorobenzenesulfonate salt (DiD) into the chloroform solution alongside other materials to form the thin lipid film. The feeding ratio of SPCm to dye was set at 50:1.

The dynamic light scattering (DLS) diameters, size distribution, polydispersity index (PDI), and zeta potential of the liposomes were measured by using a dynamic light scattering spectrometer (Malvern Zeta-sizer NanoZS90, USA).

Cryo-TEM imaging was performed using a Titan Krios G4 electron microscope to observe the morphological features of the liposomes. An aliquot of liposome suspension was deposited onto a glow-discharged carbon-coated copper grid (Cu, R2/1, 300 mesh, Quantifoil Micro Tools) and blotted for 5 s using a Mark IV Vitrobot (Thermo Fisher Scientific) at 100% humidity and 4 °C. Then, the samples underwent rapid freezing by plunging into liquid ethane, followed by cooling to 90 K in liquid nitrogen. Finally, the specimens were transferred to the Titan Krios G4 electron microscope operating at 300 kV. Images were acquired using a Falcon 4i detector at a nominal magnification of 81,000×.

4.4. Characterization of Drug-Loaded Liposomes. For the encapsulation of liraglutide (Lira) and semaglutide (Sema), drug-loaded liposomes were prepared using the modified thin-film hydration-extrusion method described above, with 4 mL of drug-containing solutions replacing deionized water during the hydration step. The feeding ratio of SPCm to Lira or Sema was maintained at 10:1.5.

To prepare budesonide-loaded liposomes (Bud@Lip), Bud was dissolved in chloroform solution alongside other materials, as the feeding ratio of SPCm to Bud was 10:0.75.

The DLS size, polydispersity index (PDI), and zeta potential of the liposomes were measured. To determine the encapsulation efficiency (EE), the liposome suspension was transferred into ultrafiltration tubes to separate free drug from drug-loaded liposomes. After the samples were rinsed with deionized water twice, the amounts of drug in the liposomes and the total drug were quantified using reverse-phase high-performance liquid chromatography (RP-HPLC, Agilent 1260 Infinity II, USA). EE was calculated using the following formula:

$$EE\% = \frac{drug \ encapsulated \ in \ liposomes}{total \ drug} \times 100$$

For drug-loading efficiency (DL) determination, a known volume of drug-loaded liposomes was freeze-dried after complete removal of the free drug, and the dry mass was weighed. DL was calculated as

$$DL\% = \frac{\text{weight of drug in liposomes}}{\text{weight of drug and liposomes}} \times 100$$

To evaluate drug release behaviors, Lira@Lip and Sema@Lip were placed in dialysis tubes (MWCO: 100 kDa) and immersed in phosphate-buffered saline (PBS, pH 1.2) under stirring for 48 h. Considering the intrinsic insolubility of Bud, the release medium of Bud@Lip was replaced with PBS (pH 7.4) containing 0.2% Tween-

20. At specific time points, 50 μ L samples were collected and analyzed using RP-HPLC.

- **4.5. Measurement of Phage Transition Temperature** (T_m) . A ten μ L portion of liposome suspensions with different hydrophilicity was placed on aluminum pans. The pans were then hermetically sealed, followed by heating at a rate of 5 °C·min⁻¹. The scans were recorded under temperatures from -40 to 60 °C via differential scanning calorimetry (DSC, METTLER TOLEDO).
- **4.6. Atomic Force Microscopy (AFM).** Prior to measurements, an aliquot of liposome suspensions was dropped onto mica, underwent initial air-drying at room temperature, and then sample hydration in an 85% humid environment. Then, Young's modulus and corresponding morphological images of liposomes were characterized using an atomic force microscope (Cypher S, Oxford Instruments, UK) in AC mode with a PTESPA-150 probe (spring constant: 5 N/m) with a scan rate of 2 Hz, and were further processed with Oxford AR software.
- **4.7. Characterization and Calculation of the Grafting Ratio of DSPE-PEG**₂₀₀₀ **on Liposomes.** To confirm the modified DSPE-PEG content in various liposomes, DSPE-PEG₂₀₀₀ was replaced with equivalent amounts of fluorescein isothiocyanate (FITC)-labeled DSPE-PEG₂₀₀₀ (FITC-DSPE-PEG₂₀₀₀) to prepare the FITC-labeled liposomes. The unincorporated FITC-DSPE-PEG₂₀₀₀ in the solution was removed by ultrafiltration using Amicon tubes (MWCO: 100 kDa, Millipore). The collected liposomes were then resuspended at the same concentration. The fluorescence emission spectra of all liposomes were measured at an excitation wavelength of 460 nm by using a Varioskan Flash Multimode Reader (Thermo Fisher Scientific, San Jose, CA, USA). Simultaneously, fluorescently labeled liposome suspensions at equivalent concentrations were photographed under normal light conditions.

In addition, we quantified the DSPE-PEG $_{2000}$ content in the liposomes. A standard curve was first established by plotting the fluorescence intensity against the concentration of FITC-labeled DSPE-PEG $_{2000}$ within a defined range. Subsequently, the resuspended FITC-labeled liposomes at the same concentration were analyzed using the microplate reader. The grafting efficiency of DSPE-PEG $_{2000}$ was calculated based on the regression curve derived from the standard curve.

- **4.8. Contact Angle Assay.** To evaluate hydrophobicity, liposome suspensions were freeze-dried and compressed into tablets, which were then adhered to glass slides. The contact angles of these samples were measured by using a contact angle measuring instrument (OCA50, DataPhysics, Germany). Quantitative analysis was performed using ImageJ software.
- **4.9. Coomassie Brilliant Blue (CBB) Adsorption Assay.** The concentrated liposome suspension was resuspended and mixed with an equal volume of Coomassie Brilliant Blue (CBB) solution (0.1 mM), with final lipid concentrations of 0.625, 1.25, and 2.5 mg·mL $^{-1}$. After vortex mixing, the mixing solution were incubated at 37 °C for 15 min with constant agitation (200 rpm). UV—vis absorption spectra were recorded between 550 and 650 nm using a Varioskan Flash Multimode Reader (Thermo Fisher Scientific, San Jose, CA, USA), and CBB solution without liposome served as the control. The wavelength shift at the absorption maximum ($\Delta\lambda$) was calculated to evaluate dye-liposome interactions.
- **4.10. Stability Evaluation of Liposomes.** The stability of liposomes following aerosolization and during pulmonary delivery was evaluated by using dynamic light scattering (DLS) and Förster resonance energy transfer (FRET) assays.

Freshly prepared liposomes were aerosolized using a microsprayer aerosolizer (BJ-PW-M, BioJane, China), and the DLS diameters of the collected liposomes were measured and compared to those of the initial formulations. Bronchoalveolar lavage fluid (BALF) was obtained as previously described, and its protein concentration was determined as 0.6 mg·mL⁻¹ via a bicinchoninic acid (BCA) assay. Liposomes were then incubated with BALF at a volume ratio of 1:2 under continuous agitation (100 rpm) at 37 °C for 12 h, with DLS measurements performed at predetermined time points.

FITC-labeled liposomes with varying surface hydrophilicity (FITC@LH Lip, FITC@MH Lip, and FITC@HH Lip) were prepared by substituting DSPE-PEG₂₀₀₀ with fluorescein isothiocyanate-labeled DSPE-PEG₂₀₀₀ (FITC-DSPE-PEG₂₀₀₀). DiI-loaded liposomes (DiI@LH Lip, DiI@MH Lip, DiI@HH Lip) and dual-labeled liposomes (named as Pre-FITC + DiI@LH Lip, Pre-FITC + DiI@ MH Lip, Pre-FITC + DiI@ HH Lip) were prepared as described above. A portion of the dual-labeled liposome suspension was aerosolized and collected (named as Post-FITC + DiI@Lips), while another portion was placed in a dialysis bag and immersed in BALF at 37 °C for 24 h before collection (named 24 h-FITC + DiI@Lips). Fluorescence intensity of single- and dual-labeled liposomes, both preand postaerosolization, as well as 24 h-incubation in BALF, was analyzed using a microplate reader at an excitation wavelength of 460 nm, and the emission spectra were recorded from 490 to 620 nm.

4.11. Pharmacokinetic Study of Liposomes with Different Hydrophobicities via Inhalation. C6-labeled liposomes were administered intratracheally to male Balb/c mice (6–8 weeks) using a microsprayer aerosolizer. The dosage was set at 1 mg·kg⁻¹. Blood samples (20 μ L) were collected from the orbital vein at predetermined intervals, and the fluorescence intensity of C6 was measured by using a microplate reader. Blood concentrations were calculated using a standard curve of fluorescence intensity versus known C6 concentrations in blood.

4.12. Lung Retention and Biodistribution after Inhalation. DiD-labeled liposomes were prepared as previously described (SPCm to DiD ratio of 50:1). After inhalation, whole-body fluorescence imaging was performed at various time points over 48 h using an IVIS Lumina III live imaging system (PerkinElmer, USA). Lung fluorescence was further semiquantitatively analyzed using region of interest (ROI) tools.

To examine pulmonary and extrapulmonary distribution in more detail, the lungs, heart, liver, spleen, and kidneys were harvested at 0 and 48 h postinhalation and subjected to fluorescence imaging. ROI fluorescence intensities were quantified by using Living Image software.

To further investigate the pulmonary distribution of liposomes, mice were aerosolized with Dil@Lips as aforementioned, followed by euthanasia and lung tissue collection at 0, 24, and 48 h postinhalation. Bronchoalveolar lavage fluid (BALF) was obtained by flushing the lungs three times with 1 mL of precold saline. Then, the fluorescence intensity of DiI in BALF was measured to quantify the retention of liposomes within the airway. For histological analysis, lungs from the 24 and 48 h groups were embedded, cryo-sectioned, and stained with FITC-WGA for mucus and DAPI for nuclei. Airway and alveolar regions were imaged using a Zeiss LSM 800 CLSM instrument (Zeiss, USA) to visualize liposome distribution.

4.13. Bioactivity Evaluation via Circular Dichroism Spectroscopy (CD). The bioactivity of aerosolized peptide drugs was assessed by using circular dichroism (CD) spectroscopy (Applied Photophysics, Chirascan-Plus, UK). Free Lira or Sema solutions (0.2 mg·mL⁻¹ in deionized water) were aerosolized via a microsprayer and collected for analysis. CD spectra were recorded from 180 to 200 nm for both aerosolized and nonaerosolized samples.

4.14. Pharmacokinetic Study and Pulmonary Distribution of Cy5-Lira@Lips via Inhalation. Lira was labeled with Cy5 as previously described. Briefly, Cy5-NHS was dissolved in DMSO, and Lira was dissolved in PBS. The two solutions were mixed at a 1:1 molar ratio, followed by the addition of 15 μ L of triethylamine, and incubated at room temperature for 8 h under light protection. The reaction mixture was then transferred to a dialysis membrane (MWCO: 1000 Da) to remove unreacted Cy5, and the final product was lyophilized. To generate a fluorescence intensity—concentration calibration curve, Cy5-Lira solutions were prepared at varying concentrations. Cy5-Lira@Lips was formulated using the thin-film hydration and extrusion method, and its particle size and polydispersity index (PDI) were characterized.

Balb/c mice were randomly assigned to four groups and inhaled with Free Cy5-Lira, Cy5-Lira@LH Lip, Cy5-Lira@MH Lip, or Cy5-Lira@HH Lip (Cy5-Lira: 5 mg·kg⁻¹). Blood samples were collected at

predetermined time points (0, 0.5, 1, 2, 4, 6, 8, 12, and 24 h), and the Cy5-Lira fluorescence intensity in blood was measured using a microplate reader. Blood concentrations were calculated based on a fluorescence intensity—concentration standard curve. Pharmacokinetic parameters were analyzed by using DAS 2.0 software. To evaluate pulmonary distribution, lungs were harvested at 48 and 72 h postinhalation and subjected to fluorescence imaging. Region of interest (ROI) fluorescence intensities were quantified by using Living Image software.

4.15. Oral Glucose Tolerance Test (OGTT) in T2DM Mice. Diabetic KKAy mice (6-8 weeks) were fed a high-fat diet (16.5% protein, 37.9% carbohydrate, 45.6% fat, Beijing HFK Bioscience, China) for 2 weeks, resulting in fasting blood glucose (FBG) levels >16.6 mmol·L⁻¹. Before the experiment, mice were fasted overnight but had free access to water. FBG was measured prior to treatment. Mice were administered inhalations of saline, free Lira solution, or Lira-loaded liposomes (Lira@LH Lip, Lira@MH Lip, and Lira@HH Lip) at an equivalent dose of 1 mg·kg⁻¹ at 3 h before glucose administration (-3 h). A glucose solution (2 g·kg⁻¹) was orally administered after 0 h. Blood glucose levels were measured at 0, 15, 30, 60, 90, and 120 min via tail vein samples using a glucose meter (Yicheng Bioelectronics, Beijing, China). A second glucose challenge was conducted under the same conditions, with blood glucose monitored for an additional 2 h. Mice receiving subcutaneous injections of free Lira (0.2 mg·kg⁻¹) served as a positive control. Incremental blood glucose level (ΔBGL) values were calculated by subtracting the initial FBG, and the incremental area under the curve (iAUC) was determined. Relative pharmacological bioavailability (RPA) was calculated using

$$RPA\% = \frac{iAUC(inh) \times dose(sc)}{iAUC(sc) \times dose(inh)} \times 100$$

For Sema@Lip, the administered Sema dose was halved and procedures were conducted in parallel with those for Lira@Lip.

4.16. Establishment of an Acute Allergic Asthma Model. To establish an acute allergic asthma model, male BALB/c mice (6–8 weeks) were sensitized twice and challenged three times with ovalbumin (OVA). On days 0 and 7, mice were intraperitoneally injected with a suspension containing 50 μ g OVA and 2 mg Al(OH)₃. Prior to injection, the OVA and Al(OH)₃ were dispersed in sterile saline and stirred for 4 h at 4 °C to ensure complete adsorption of the OVA onto Al(OH)₃. Subsequently, mice were challenged with an OVA solution (2 mg·kg⁻¹) via inhalation on days 14–16.

4.17. Lung Retention in Acute Allergic Asthmatic Mice. To evaluate the pulmonary retention of liposomes with varying hydrophilicity, asthmatic mice were intratracheally aerosolized with DiD@Lip and free DiD as described previously. Fluorescence signals were monitored using an IVIS system at multiple time points. Lung tissues were harvested at 48 and 72 h postinhalation for fluorescence imaging, and ROIs were quantified using IVIS software.

4.18. Pharmacokinetic Study and Pulmonary Distribution of Bud@Lips in Acute Allergic Asthmatic Mice. The acute allergic asthma model mice were administered aerosolized formulations of Free Bud, Bud@LH Lip, Bud@MH Lip, and Bud@HH Lip (budesonide: 2 mg·kg⁻¹). Blood samples were collected at predetermined time points (0, 0.25, 0.5, 1, 2, 4, 6, 8, 12, 24, 48, and 72 h), centrifuged at 3500 rpm for 5 min at 4 °C to isolate plasma, and stored at-80 °C until analysis. Plasma budesonide levels were quantified by using high-performance liquid chromatography (HPLC) as previously described. Briefly, 200 μ L of plasma was mixed with 40 µL of phosphate buffer (pH 3.2) and vortexed for 1 min, followed by the addition of 1 mL ethyl acetate and vortexing for an additional 3 min. The mixture was centrifuged at 10,000 rpm for 5 min at 4 °C, and the upper organic phase was collected, evaporated under a nitrogen stream at 40 $^{\circ}$ C for 20 min, and redissolved in 50 μ L methanol. The sample was vortexed for 3 min and centrifuged at 10,000 rpm for 5 min at 4 °C, and the supernatant was analyzed by HPLC.

For pulmonary budesonide quantification, freshly excised lung tissue was accurately weighed and transferred to a 2 mL grinding tube. The tissue was homogenized in 500 μL of PBS, and the resulting homogenate was centrifuged at 3500 rpm for 5 min at 4 °C. A 500 μL aliquot of the supernatant was collected and processed following the same extraction protocol as for plasma samples.

4.19. In Vivo Anti-Asthmatic Efficacy of Bud@Lip. To evaluate the therapeutic efficacy of Bud@Lip, sensitized male BALB/c mice were randomly divided into five groups for intratracheal administration with saline, free Bud, Bud@LH Lip, Bud@MH Lip, and Bud@HH Lip via inhalation on day 14. Subsequently, mice were challenged with OVA solution at 2 h, followed by additional challenges on days 15 and 16. Normal control mice received sterile saline throughout the experiment. On day 17, all mice were euthanized, and lung tissues were harvested for further analysis. Lung tissues were lavaged three times with 0.5 mL of cold saline to collect BALF, and the supernatant was obtained after centrifugation (1500 rpm, 10 min, 4 °C). Cytokine levels (IL-4, IL-5, and IL-13) in BALF were quantified using enzyme-linked immunosorbent assay (ELISA) kits according to the manufacturer's protocols. Lung sections were stained with hematoxylin and eosin (H&E) and periodic acid-Schiff (PAS) stain to evaluate mucus secretion and histopathological changes.

4.20. Mucus Penetration Assessment. To evaluate the transmucus penetration ability of liposomes, artificial lung mucus was prepared as described in previous studies. Briefly, 500 mg of DNA, 250 μ L of aseptic yolk milk, 250 mg of mucin, 0.295 mg of DTPA, 250 mg of NaCl, 110 mg of KCl, and 1 mL of RPMI were added to 50 mL of water under stirring to form a homogeneous mixture.

Then, artificial mucus was coated onto the apical side of the transwell membranes, and basolateral chambers were filled with 800 μ L of PBS for equilibration. After 30 min, the apical medium was added with 200 μ L of DiI-labeled liposomes. At 0, 0.25, 0.5, 1, 1.5, 2, and 2.5 h, 50 μ L of samples were collected from the basolateral chamber and replaced with fresh buffer. Fluorescence intensity was measured as described previously, and the apparent permeability coefficient ($P_{\rm app}$) was calculated using the following equation:

$$P_{\rm app} = \frac{\mathrm{d}t}{\mathrm{d}Q} \times \frac{1}{A \times C_0}$$

where dQ/dt is the flux rate of DiI from donor side to acceptor side, C_0 is the initial concentration of DiI in the donor compartment, and A is the membrane area (cm²).

4.21. Cellular Uptake and Mechanism Study. For cellular uptake studies, NCI-H441 cells were seeded on coverslips at a density of 5×10^4 cells per well and cultured for 4 d. Before the experiment, the medium was removed, and cells were washed twice with PBS. The cells were then incubated with Dil@Lip for 3 h, fixed with 4% paraformaldehyde, and stained with DAPI. Fluorescence imaging was performed using a confocal laser-scanning microscope (CLSM).

To assess the cell-binding ability, NCI-H441 or Calu-3 cells were seeded in 96-well plates and cultured for 4 d. After removing the culture medium and washing with cold PBS, cells were treated with precooled DiI-labeled liposomes at various concentrations for 1 h at 4 °C. After gently washing with cold PBS, 100 µL of DMSO was added to dissolve membrane-bound DiI@Lip. Fluorescence intensity was measured using a microplate reader, and cell numbers were determined by using the Alamar Blue assay.

To investigate the internalization mechanism, NCI-H441 was pretreated with specific endocytic inhibitors for 30 min before incubating with Dil@Lip for 3 h. Cells without inhibitors served as the control. Fluorescence intensity was measured as described above.

4.22. Intracellular Trafficking and Exocytosis in NCI-H441 Cells. To evaluate colocalization with intracellular organelles, NCI-H441 cells on coverslips were incubated with C6-loaded liposomes for 2 h. Lyso-Tracker, ER-Tracker, and Golgi-Tracker dyes were used to label lysosomes, endoplasmic reticulum (ER), and the Golgi apparatus, respectively, following the manufacturers' protocols. DAPI was used to stain the nuclei. Colocalization efficiency, represented by

Pearson's correlation coefficient (PCC), was calculated using ImageJ software.

To study the exocytosis rate, NCI-H441 cells were incubated with Dil@Lips for 2 h. Afterward, the blank culture medium was added to facilitate exocytosis. Cells without the exocytosis step served as the control. Fluorescence intensity was measured, and exocytosis efficiency was calculated as the ratio of fluorescence intensity in exocytosed cells to that in control cells.

4.23. Transcellular Transport Study. NCI-H441 or Calu-3 cells were seeded on transwell inserts at a density of cells per well and cultured for 14–16 d. A transepithelial electrical resistance (TEER) value of >300 $\Omega \cdot \text{cm}^2$ for NCI-H441 cells or >600 $\Omega \cdot \text{cm}^2$ for Calu-3 cells was confirmed using a Millicell-ERS system (Millipore, USA). Before the study, cell monolayers were equilibrated with prewarmed Hank's balanced salt solution (HBSS) for 30 min.

The apical medium was replaced with 200 μ L of DiI-labeled liposomes. At predetermined intervals, 50 μ L of basolateral medium was collected and replaced with a fresh buffer. Fluorescence intensity was measured as described previously, and the apparent permeability coefficient ($P_{\rm app}$) was calculated using the following formula:

$$P_{\rm app} = \frac{\mathrm{d}t}{\mathrm{d}Q} \times \frac{1}{A \times C_0}$$

where dQ/dt is the flux rate of DiI from donor side to acceptor side, C_0 is the initial concentration of DiI in the donor compartment, and A is the membrane area (cm²).

4.24. Phagocytosis of Liposomes by Macrophages. To investigate macrophage uptake of liposomes with varying hydrophobicity, RAW264.7 cells were seeded into 12-well plates and incubated with DiI@Lip for 3 h. Phagocytosis was evaluated using a Beckman CytoFLEX flow cytometer (Beckman Coulter, Shanghai, China).

4.25. Biosafety Evaluation of Liposomes. For cell viability studies, NCI-H441, Calu-3, and TC-1 cells were seeded into 96-well plates and incubated with blank liposomes at varying concentrations for 3 h, followed by incubation with a resazurin solution (10 μ g·mL⁻¹) for 1 h. Fluorescence intensity was measured as described previously.

For hemolysis analysis, red blood cells (RBCs) were extracted as previously described and mixed with blank liposomes at various concentrations in a volume ratio of 1:1. The mixtures were incubated at 37 $^{\circ}$ C for 3 h. After centrifugation (1500 rpm, 10 min, 37 $^{\circ}$ C), the absorbance of the supernatant was measured at 545 nm. RBCs treated with saline and 0.1% Triton-X 100 served as negative and positive controls, respectively. The hemolysis ratio was calculated using the following equation:

$$\mbox{hemolysis ratio\%} = \frac{A_{\mbox{liposomes}} - A_{\mbox{saline}}}{A_{\mbox{triton}} - A_{\mbox{saline}}} \times 100$$

For in vivo biosafety assessment, male ICR mice (6–8 week) were randomly divided into four groups and exposed to saline, blank LH Lip, MH Lip, or HH Lip at the highest dose used in the study (SPCm: $10~{\rm mg\cdot kg^{-1}}$ in $50~\mu{\rm L}$ suspension) via inhalation every 3 days for 1 week. Body weight was recorded daily. At the end of the study, serum and whole blood samples were collected for blood biochemistry and complete blood count analysis. Major organs were harvested for histological evaluation via hematoxylin-eosin (H&E) staining. Inflammatory cytokine levels, including TNF- α , IL-6, and IL- 1β in BALF, were quantified using ELISA kits according to the manufacturer's instructions.

4.26. Statistical Analysis. All statistical analyses were performed using SPSS 23.0 software, and data are presented as mean \pm standard deviation (SD). Statistical significance between multiple groups was determined using one-way ANOVA followed by Tukey's multiple comparisons test. For comparisons between two groups, an unpaired Student's t test was used. Statistical significance was indicated as follows: (*, #, &, \$) P < 0.05, (**, ##, &&, \$\$) P < 0.01, (***, ###, &&&, \$\$\$) P < 0.0001.

ASSOCIATED CONTENT

Supporting Information

The Supporting Information is available free of charge at https://pubs.acs.org/doi/10.1021/acsnano.5c05745.

Additional figures referenced in the main text; tabulated characterization data of Sema@Lips and plasmatic pharmacokinetic parameters of Bud@Lips; physical images of FITC-labeled liposomes, aerosolization performance and aerodynamic diameter analysis; FRET spectra of liposomes; IVIS imaging and quantitative analysis of extra-pulmonary organ distribution, surface hydrophobicity evaluation of drug-loaded liposomes; particle size distributions; blood concentration profiles; detailed pharmacokinetic parameters; pulmonary accumulation of Cy5-Lira@Lips after inhalation; bioactivity assessment of aerosolized sema; OGTT blood glucose levels and iAUC of Sema@Lipstreated T2DM mice; confocal images of tight junction protein expression; intracellular trafficking analysis in NCI-H441 cells; cellular viability assay in TC-1 cells; and hemolytic analysis of liposomes (PDF)

AUTHOR INFORMATION

Corresponding Author

Yuan Huang — Key Laboratory of Drug-Targeting and Drug Delivery System of the Education Ministry and Sichuan Province, Sichuan Engineering Laboratory for Plant-Sourced Drug and Sichuan Research Center for Drug Precision Industrial Technology, West China School of Pharmacy, Sichuan University, Chengdu 610041, China; orcid.org/0000-0003-3410-8602; Phone: + 8628 85501617; Email: huangyuan0@163.com

Authors

- Xi Liu Key Laboratory of Drug-Targeting and Drug Delivery System of the Education Ministry and Sichuan Province, Sichuan Engineering Laboratory for Plant-Sourced Drug and Sichuan Research Center for Drug Precision Industrial Technology, West China School of Pharmacy, Sichuan University, Chengdu 610041, China
- Lie Zhang Key Laboratory of Drug-Targeting and Drug Delivery System of the Education Ministry and Sichuan Province, Sichuan Engineering Laboratory for Plant-Sourced Drug and Sichuan Research Center for Drug Precision Industrial Technology, West China School of Pharmacy, Sichuan University, Chengdu 610041, China
- Sa Li Key Laboratory of Drug-Targeting and Drug Delivery System of the Education Ministry and Sichuan Province, Sichuan Engineering Laboratory for Plant-Sourced Drug and Sichuan Research Center for Drug Precision Industrial Technology, West China School of Pharmacy, Sichuan University, Chengdu 610041, China
- Liyun Xing Key Laboratory of Drug-Targeting and Drug Delivery System of the Education Ministry and Sichuan Province, Sichuan Engineering Laboratory for Plant-Sourced Drug and Sichuan Research Center for Drug Precision Industrial Technology, West China School of Pharmacy, Sichuan University, Chengdu 610041, China
- Mingjie Ni Key Laboratory of Drug-Targeting and Drug Delivery System of the Education Ministry and Sichuan Province, Sichuan Engineering Laboratory for Plant-Sourced Drug and Sichuan Research Center for Drug Precision

Industrial Technology, West China School of Pharmacy, Sichuan University, Chengdu 610041, China

Minyi Huang — Key Laboratory of Drug-Targeting and Drug Delivery System of the Education Ministry and Sichuan Province, Sichuan Engineering Laboratory for Plant-Sourced Drug and Sichuan Research Center for Drug Precision Industrial Technology, West China School of Pharmacy, Sichuan University, Chengdu 610041, China

Complete contact information is available at: https://pubs.acs.org/10.1021/acsnano.5c05745

Author Contributions

Y.H.: designed the experimental protocol. X.L.: performed the experimental work, analyzed the data, and wrote the manuscript. L.Z. and S.L.: contributed to the HPLC analysis, animal experimental tests and data analysis. L.X.: modified the manuscript. M.N.: contributed to the animal experimental tests. M.H.: participated in preparation and characterization of delivery system. All authors have given approval to the final version of the manuscript.

Note

The authors declare no competing financial interest.

ACKNOWLEDGMENTS

We are grateful for the financial support from the Regional Innovation and Development Joint Fund of the National Natural Science Foundation of China (grant numbers: U22A20356). We also thank the Tianfu Jincheng laboratory Cryo-EM center for the cryo-EM.

REFERENCES

- (1) Zhang, Y. B.; Xu, D.; Bai, L.; Zhou, Y. M.; Zhang, H.; Cui, Y. L. A Review of Non-Invasive Drug Delivery through Respiratory Routes. *Pharmaceutics* **2022**, *14* (9), *26*.
- (2) Ho, D. K.; Nichols, B. L. B.; Edgar, K. J.; Murgia, X.; Loretz, B.; Lehr, C. M. Challenges and Strategies in Drug Delivery Systems for Treatment of Pulmonary Infections. *Eur. J. Pharm. Biopharm.* **2019**, 144, 110–124.
- (3) Wang, W.; Huang, Z.; Huang, Y.; Zhang, X.; Huang, J.; Cui, Y.; Yue, X.; Ma, C.; Fu, F.; Wang, W.; Wu, C.; Pan, X. Pulmonary Delivery Nanomedicines Towards Circumventing Physiological Barriers: Strategies and Characterization Approaches. *Adv. Drug Delivery Rev.* 2022, 185, No. 114309.
- (4) Siekmeier, R.; Scheuch, G. Treatment of Systemic Diseases by Inhalation of Biomolecule Aerosols. *J. Physiol. Pharmacol.* **2009**, *60*, 15–26
- (5) He, S. Q.; Gui, J. J.; Xiong, K.; Chen, M. W.; Gao, H. L.; Fu, Y. A Roadmap to Pulmonary Delivery Strategies for the Treatment of Infectious Lung Diseases. *J. Nanobiotechnol.* **2022**, 20 (1), 101.
- (6) Adjei, A.; Gupta, P. Pulmonary Delivery of Therapeutic Peptides and Proteins. *J. Controlled Release* **1994**, 29 (3), 361–373.
- (7) Newman, S. P. Drug Delivery to the Lungs: Challenges and Opportunities. *Ther. Delivery* **2017**, 8 (8), 647–661.
- (8) Liu, H. F.; Shan, X. S.; Yu, J. J.; Li, X.; Hu, L. D. Recent Advances in Inhaled Formulations and Pulmonary Insulin Delivery Systems. *Curr. Pharm. Biotechnol.* **2020**, *21* (3), 180–193.
- (9) Patton, J. S.; Trinchero, P.; Platz, R. M. Bioavailability of Pulmonary Delivered Peptides and Proteins: A-Interferon, Calcitonins and Parathyroid Hormones. *J. Controlled Release* **1994**, 28 (1–3), 79–85.
- (10) Wang, B.; Wang, L.; Yang, Q.; Zhang, Y. M.; Qinglai, T.; Yang, X. M.; Xiao, Z.; Lei, L. J.; Li, S. S. Pulmonary Inhalation for Disease Treatment: Basic Research and Clinical Translations. *Mater. Today Bio* **2024**, 25, No. 100966.

- (11) Gaikwad, S. S.; Pathare, S. R.; More, M. A.; Waykhinde, N. A.; Laddha, U. D.; Salunkhe, K. S.; Kshirsagar, S. J.; Patil, S. S.; Ramteke, K. H. Dry Powder Inhaler with the Technical and Practical Obstacles, and Forthcoming Platform Strategies. *J. Controlled Release* **2023**, 355, 292–311.
- (12) Heida, R.; Hinrichs, W. L. J.; Frijlink, H. W. Inhaled Vaccine Delivery in the Combat against Respiratory Viruses: A 2021 Overview of Recent Developments and Implications for COVID-19. *Expert Rev. Vaccines* **2022**, 21 (7), 957–974.
- (13) Plaunt, A. J.; Nguyen, T. L.; Corboz, M. R.; Malinin, V. S.; Cipolla, D. C. Strategies to Overcome Biological Barriers Associated with Pulmonary Drug Delivery. *Pharmaceutics* **2022**, *14* (2), 302.
- (14) Kunde, S. S.; Ghosh, R.; Wairkar, S. Emerging Trends in Pulmonary Delivery of Biopharmaceuticals. *Drug Discovery Today* **2022**, *27* (5), 1474–1482.
- (15) Kuzmov, A.; Minko, T. Nanotechnology Approaches for Inhalation Treatment of Lung Diseases. *J. Controlled Release* **2015**, 219, 500–518.
- (16) Afzal, O.; Altamimi, A. S. A.; Nadeem, M. S.; Alzarea, S. I.; Almalki, W. H.; Tariq, A.; Mubeen, B.; Murtaza, B. N.; Iftikhar, S.; Riaz, N.; Kazmi, I. Nanoparticles in Drug Delivery: From History to Therapeutic Applications. *Nanomaterials* **2022**, *12* (24), 4494.
- (17) Park, H.; Otte, A.; Park, K. Evolution of Drug Delivery Systems: From 1950 to 2020 and Beyond. *J. Controlled Release* **2022**, 342, 53–65.
- (18) Liu, Q. Y.; Zhang, X. R.; Xue, J. W.; Chai, J. J.; Qin, L.; Guan, J.; Zhang, X.; Mao, S. R. Exploring the Intrinsic Micro-/Nanoparticle Size on Their in Vivo Fate after Lung Delivery. *J. Controlled Release* **2022**, 347, 435–448.
- (19) Zhao, J.; Qin, L.; Song, R. X.; Su, J.; Yuan, Y.; Zhang, X.; Mao, S. R. Elucidating Inhaled Liposome Surface Charge on Its Interaction with Biological Barriers in the Lung. *Eur. J. Pharm. Biopharm.* **2022**, 172, 101–111.
- (20) Nie, D.; Liu, C.; Yu, M. R.; Jiang, X. H.; Wang, N.; Gan, Y. Elasticity Regulates Nanomaterial Transport as Delivery Vehicles: Design, Characterization, Mechanisms and State of the Art. *Biomaterials* **2022**, *291*, No. 121879.
- (21) Liu, Q. Y.; Guan, J.; Song, R. X.; Zhang, X.; Mao, S. R. Physicochemical Properties of Nanoparticles Affecting Their Fate and the Physiological Function of Pulmonary Surfactants. *Acta Biomater.* **2022**, *140*, 76–87.
- (22) Liu, Q. Y.; Guan, J.; Qin, L.; Zhang, X.; Mao, S. R. Physicochemical Properties Affecting the Fate of Nanoparticles in Pulmonary Drug Delivery. *Drug Discovery Today* **2020**, 25 (1), 150–159.
- (23) Yu, Y. L.; Li, S. J.; Yao, Y.; Shen, X. R.; Li, L.; Huang, Y. Increasing Stiffness Promotes Pulmonary Retention of Ligand-Directed Dexamethasone-Loaded Nanoparticle for Enhanced Acute Lung Inflammation Therapy. *Bioact. Mater.* **2023**, *20*, 539–547.
- (24) Wu, L.; Bai, Y. L.; Liu, M.; Li, L.; Shan, W.; Zhang, Z. R.; Huang, Y. Transport Mechanisms of Butyrate Modified Nanoparticles: Insight into "Easy Entry, Hard Transcytosis" of Active Targeting System in Oral Administration. *Mol. Pharmaceutics* **2018**, 15 (9), 4273–4283.
- (25) Zhu, X.; Wu, J.; Shan, W.; Tao, W.; Zhao, L. L.; Lim, J. M.; D'Ortenzio, M.; Karnik, R.; Huang, Y.; Shi, J. J.; Farokhzad, O. C. Polymeric Nanoparticles Amenable to Simultaneous Installation of Exterior Targeting and Interior Therapeutic Proteins. *Angew. Chem., Int. Ed. Engl.* **2016**, *55* (10), 3309–3312.
- (26) Shan, W.; Zhu, X.; Liu, M.; Li, L.; Zhong, J. J.; Sun, W.; Zhang, Z. R.; Huang, Y. Overcoming the Diffusion Barrier of Mucus and Absorption Barrier of Epithelium by Self-Assembled Nanoparticles for Oral Delivery of Insulin. ACS Nano 2015, 9 (3), 2345–2356.
- (27) Liu, M.; Zhang, J.; Zhu, X.; Shan, W.; Li, L.; Zhong, J. J.; Zhang, Z. R.; Huang, Y. Efficient Mucus Permeation and Tight Junction Opening by Dissociable "Mucus-Inert" Agent Coated Trimethyl Chitosan Nanoparticles for Oral Insulin Delivery. J. Controlled Release 2016, 222, 67–77.

- (28) Yan, X.; Sha, X. Y. Nanoparticle-Mediated Strategies for Enhanced Drug Penetration and Retention in the Airway Mucosa. *Pharmaceutics* **2023**, *15* (10), 2457.
- (29) Haque, S.; McLeod, V. M.; Jones, S.; Fung, S.; Whittaker, M.; McIntosh, M.; Pouton, C.; Owen, D. J.; Porter, C. J. H.; Kaminskas, L. M. Effect of Increased Surface Hydrophobicity Via Drug Conjugation on the Clearance of Inhaled PEGylated Polylysine Dendrimers. *Eur. J. Pharm. Biopharm.* **2017**, *119*, 408–418.
- (30) Watchorn, J.; Clasky, A. J.; Prakash, G.; Johnston, I. A. E.; Chen, P. Z.; Gu, F. X. Untangling Mucosal Drug Delivery: Engineering, Designing, and Testing Nanoparticles to Overcome the Mucus Barrier. ACS Biomater. Sci. Eng. 2022, 8 (4), 1396–1426.
- (31) Raviv, S. A.; Alyan, M.; Egorov, E.; Zano, A.; Harush, M. Y.; Pieters, C.; Korach-Rechtman, H.; Saadya, A.; Kaneti, G.; Nudelman, I.; Farkash, S.; Flikshtain, O. D.; Mekies, L. N.; Koren, L.; Gal, Y.; Dor, E.; Shainsky, J.; Shklover, J.; Adir, Y.; Schroeder, A. Lung Targeted Liposomes for Treating ARDS. *J. Controlled Release* **2022**, 346, 421–433.
- (32) Bassetti, M.; Vena, A.; Russo, A.; Peghin, M. Inhaled Liposomal Antimicrobial Delivery in Lung Infections. *Drugs* **2020**, *80* (13), 1309–1318.
- (33) Xiao, X.; Zhang, L.; Ni, M. J.; Liu, X.; Xing, L. Y.; Wu, L. C.; Zhou, Z.; Li, L.; Wen, J. Y.; Huang, Y. Enhanced Oral and Pulmonary Delivery of Biomacromolecules Via Amplified Transporter Targeting. *J. Controlled Release* **2024**, *370*, 152–167.
- (34) Wu, R. A.; Wu, Z. H.; Xing, L. Y.; Liu, X.; Wu, L.; Zhou, Z.; Li, L.; Huang, Y. Mimicking Natural Cholesterol Assimilation to Elevate the Oral Delivery of Liraglutide for Type II Diabetes Therapy. *Asian J. Pharm. Sci.* **2022**, *17* (5), 653–665.
- (35) Ortiz, M.; Coutinho, D. D.; Ciambarella, B. T.; de Souza, E. T.; D'Almeida, A. P. L.; Durli, T. L.; Silva, P.; Bernardi, A.; Sonvico, F.; Pohlmann, A. R.; Martins, M. A.; Guterres, S. S. Intranasal Administration of Budesonide-Loaded Nanocapsule Microagglomerates as an Innovative Strategy for Asthma Treatment. *Drug Delivery Transl. Res.* **2020**, *10* (6), 1700–1715.
- (36) Huckaby, J. T.; Lai, S. K. PEGylation for Enhancing Nanoparticle Diffusion in Mucus. *Adv. Drug Delivery Rev.* **2018**, 124, 125–139.
- (37) Wu, L.; Shan, W.; Zhang, Z. R.; Huang, Y. Engineering Nanomaterials to Overcome the Mucosal Barrier by Modulating Surface Properties. *Adv. Drug Delivery Rev.* **2018**, *124*, 150–163.
- (38) Liu, X.; Wu, R. N.; Li, Y. T.; Wang, L. L.; Zhou, R.; Li, L.; Xiang, Y. C.; Wu, J. W.; Xing, L. Y.; Huang, Y. Angiopep-2-Functionalized Nanoparticles Enhance Transport of Protein Drugs across Intestinal Epithelia by Self-Regulation of Targeted Receptors. *Biomater. Sci.* **2021**, *9* (8), 2903–2916.
- (39) Yu, M. R.; Song, W. Y.; Tian, F. L.; Dai, Z.; Zhu, Q. L.; Ahmad, E.; Guo, S. Y.; Zhu, C. L.; Zhong, H. J.; Yuan, Y. C.; Zhang, T.; Yi, X.; Shi, X. H.; Gan, Y.; Gao, H. J. Temperature- and Rigidity-Mediated Rapid Transport of Lipid Nanovesicles in Hydrogels. *Proc. Natl. Acad. Sci. U. S. A.* 2019, 116 (12), 5362–5369.
- (40) Chen, Y.; Lin, S.; Wang, L.; Zhang, Y.; Chen, H.; Fu, Z.; Zhang, M.; Luo, H.; Liu, J.; Chen, Y. M.; Lin, S. S.; Wang, L.; Zhang, Y. F.; Chen, H.; Fu, Z. Z.; Zhang, M. M.; Luo, H. L.; Liu, J. Y. Reinforcement of the Intestinal Mucosal Barrier Via Mucus-Penetrating PEGylated Bacteria. *Nat. Biomed. Eng.* **2024**, *8* (7), 823–841.
- (41) Xiao, Y.; Wiesner, M. R. Characterization of Surface Hydrophobicity of Engineered Nanoparticles. *J. Hazard. Mater.* **2012**, 215, 146–151.
- (42) Beck, C.; Ramanujam, D.; Vaccarello, P.; Widenmeyer, F.; Feuerherd, M.; Cheng, C. C.; Bomhard, A.; Abikeeva, T.; Schädler, J.; Sperhake, J. P.; Graw, M.; Safi, S.; Hoffmann, H.; Staab-Weijnitz, C. A.; Rad, R.; Protzer, U.; Frischmuth, T.; Engelhardt, S. Trimannose-Coupled Antimir-21 for Macrophage-Targeted Inhalation Treatment of Acute Inflammatory Lung Damage. *Nat. Commun.* 2023, 14 (1), 4564.
- (43) Zhang, H.; Zhu, W. J.; Jin, Q. T.; Pan, F.; Zhu, J. F.; Liu, Y. B.; Chen, L. F.; Shen, J. J.; Yang, Y.; Chen, Q.; Liu, Z. Inhalable

- Nanocatchers for SARS-Cov-2 Inhibition. *Proc. Natl. Acad. Sci. U. S. A.* **2021**, *118* (29), No. e2102957118.
- (44) Wang, H. R.; Luo, S.; Xie, M. X.; Chen, Z.; Zhang, Y. M.; Xie, Z. Q.; Zhang, Y. S.; Zhang, Y.; Yang, L.; Wu, F. H.; Chen, X. Y.; Du, G. S.; Zhao, J. C.; Sun, X. ACE2 Receptor-Targeted Inhaled Nanoemulsions Inhibit SARS-Cov-2 and Attenuate Inflammatory Responses. *Adv. Mater.* **2024**, *36* (14), No. e2311537.
- (45) Brown, E.; Wilding, J. P. H.; Barber, T. M.; Alam, U.; Cuthbertson, D. J. Weight Loss Variability with SGLT2 Inhibitors and GLP-1 Receptor Agonists in Type 2 Diabetes Mellitus and Obesity: Mechanistic Possibilities. *Obes. Rev.* **2019**, *20* (6), 816–828.
- (46) Nauck, M. A.; Quast, D. R.; Wefers, J.; Meier, J. J. GLP-1 Receptor Agonists in the Treatment of Type 2 Diabetes-State-of-the-Art. *Mol. Metab.* **2020**, *46*, No. 101102.
- (47) Vargason, A. M.; Anselmo, A. C.; Mitragotri, S. The Evolution of Commercial Drug Delivery Technologies. *Nat. Biomed. Eng.* **2021**, 5 (9), 951–967.
- (48) Zhang, J. X.; Zhou, J. C.; Zhang, T. T.; Niu, Z. X.; Wang, J.; Guo, J. M.; Li, Z. G.; Zhang, Z. Z. Facile Fabrication of an Amentoflavone-Loaded Micelle System for Oral Delivery to Improve Bioavailability and Hypoglycemic Effects in Kkay Mice. ACS Appl. Mater. Interfaces 2019, 11 (13), 12904–12913.
- (49) Knudsen, L. B.; Lau, J. The Discovery and Development of Liraglutide and Semaglutide. Front. Endocrinol. 2019, 10, 155.
- (50) Chellappan, D. K.; Prasher, P.; Saravanan, V.; Yee, V. S. V.; Chi, W. C. W.; Wong, J. W.; Wong, J. K.; Wong, J. T.; Wan, W.; Chellian, J.; Molugulu, N.; Prabu, S. L.; Ibrahim, R.; Darmarajan, T.; Candasamy, M.; Singh, P. K.; Mishra, V.; Shastri, M. D.; Zacconi, F. C.; Chakraborty, A.; et al. Protein and Peptide Delivery to Lungs by Using Advanced Targeted Drug Delivery. *Chem.-Biol. Interact.* 2022, 351, No. 109706.
- (51) Al-Tabakha, M. M. Future Prospect of Insulin Inhalation for Diabetic Patients: The Case of Afrezza Versus Exubera. *J. Controlled Release* **2015**, *215*, 25–38.
- (52) Boboltz, A.; Kumar, S.; Duncan, G. A. Inhaled Drug Delivery for the Targeted Treatment of Asthma. *Adv. Drug Delivery Rev.* **2023**, 198, No. 114858.
- (53) Yu, Y. L.; Ni, M. J.; Zheng, Y. X.; Huang, Y. Airway Epithelial-Targeted Nanoparticle Reverses Asthma in Inhalation Therapy. *J. Controlled Release* **2024**, *367*, 223–234.
- (54) Lourenço, L. O.; Ribeiro, A. M.; Lopes, F.; Tibério, I.; Tavares-de-Lima, W.; Prado, C. M. Different Phenotypes in Asthma: Clinical Findings and Experimental Animal Models. *Clin. Rev. Allergy Immunol.* **2022**, *62* (1), 240–263.
- (55) Zuo, X.; Gu, Y. N.; Guo, X. P.; Zheng, W. X.; Zheng, H. Y.; An, Y. M.; Xu, C. A.; Wang, F. Preparation of Budesonide-Loaded Liposomal Nanoparticles for Pulmonary Delivery and Their Therapeutic Effect in OVA-Induced Asthma in Mice. *Int. J. Nanomed.* **2024**, *19*, 673–688.
- (56) Li, J. Q.; Zheng, H. L.; Xu, E. Y.; Moehwald, M.; Chen, L.; Zhang, X.; Mao, S. R. Inhalable PLGA Microspheres: Tunable Lung Retention and Systemic Exposure Via Polyethylene Glycol Modification. *Acta Biomater.* **2021**, *123*, 325–334.
- (57) Huck, B. C.; Murgia, X.; Frisch, S.; Hittinger, M.; Hidalgo, A.; Loretz, B.; Lehr, C. M. Models Using Native Tracheobronchial Mucus in the Context of Pulmonary Drug Delivery Research: Composition, Structure and Barrier Properties. *Adv. Drug Delivery Rev.* **2022**, *183*, No. 114141.
- (58) Sakagami, M. In Vitro, Ex Vivo and in Vivo Methods of Lung Absorption for Inhaled Drugs. *Adv. Drug Delivery Rev.* **2020**, *161*, 63–74
- (59) Guo, Y. Y.; Ma, Y. B.; Chen, X.; Li, M.; Ma, X. H.; Cheng, G.; Xue, C. Y.; Zuo, Y. Y.; Sun, B. B. Mucus Penetration of Surface-Engineered Nanoparticles in Various pH Microenvironments. *ACS Nano* **2023**, *17*, 2813–2828.
- (60) Ren, H.; Birch, N. P.; Suresh, V. An Optimised Human Cell Culture Model for Alveolar Epithelial Transport. *PLoS One* **2016**, *11* (10), No. e0165225.

- (61) Salomon, J. J.; Muchitsch, V. E.; Gausterer, J. C.; Schwagerus, E.; Huwer, H.; Daum, N.; Lehr, C. M.; Ehrhardt, C. The Cell Line Ncl-H441 Is a Useful in Vitro Model for Transport Studies of Human Distal Lung Epithelial Barrier. *Mol. Pharmaceutics* **2014**, *11* (3), 995–1006
- (62) Gumbleton, M. Caveolae as Potential Macromolecule Trafficking Compartments within Alveolar Epithelium. *Adv. Drug Delivery Rev.* **2001**, 49 (3), 281–300.
- (63) Verma, A.; Uzun, O.; Hu, Y. H.; Hu, Y.; Han, H. S.; Watson, N.; Chen, S. L.; Irvine, D. J.; Stellacci, F. Surface-Structure-Regulated Cell-Membrane Penetration by Monolayer-Protected Nanoparticles. *Nat. Mater.* **2013**, *12* (4), 376–376.
- (64) Shima, F.; Akagi, T.; Akashi, M. The Role of Hydrophobicity in the Disruption of Erythrocyte Membrane by Nanoparticles Composed of Hydrophobically Modified Poly(Γ-Glutamic Acid). *J. Biomater. Sci.-Polym. Ed.* **2014**, 25 (2), 203–210.
- (65) Zhang, J. W.; Chen, Z.; Shan, D.; Wu, Y.; Zhao, Y.; Li, C.; Shu, Y.; Linghu, X.; Wang, B. Q. Adverse Effects of Exposure to Fine Particles and Ultrafine Particles in the Environment on Different Organs of Organisms. *J. Environ. Sci.* **2024**, *135*, 449–473.
- (66) Haldar, S.; Muralidaran, Y.; Miguez, D.; Mulla, S. I.; Mishra, P. Eco-Toxicity of Nano-Plastics and Its Implication on Human Metabolism: Current and Future Perspective. *Sci. Total Environ.* **2023**, *861*, No. 160571.